AIAA JOURNAL
Vol. 54, No. 12, December 2016

Segmented Bayesian Calibration of Multidisciplinary Models

Erin C. DeCarlo*
Vanderbilt University, Nashville, Tennessee 37235
Benjamin P. Smarslok†
U.S. Air Force Research Laboratory, Wright–Patterson Air Force Base, Ohio 45433
and
Sankaran Mahadevan‡
Vanderbilt University, Nashville, Tennessee 37235

DOI: 10.2514/1.J054960

This paper investigates Bayesian model calibration for multidisciplinary problems that involve several disciplinary models and multiple sources of data regarding individual and combined physics. A segmented approach is explored as an alternative to simultaneous calibration of the parameters and discrepancy terms of all the component models. Simultaneous Bayesian calibration requires conducting inference on all uncertain parameters using all models and data concurrently. This can lead to significant computational burden and ambiguity regarding each individual model's contribution to the overall prediction uncertainty. Segmented Bayesian model calibration is first investigated with two illustrative mathematical examples and the performance of this strategy is examined for different characteristics of the problem (i.e., model dependence and data availability). The Kullback–Leibler divergence and the Bayes factor metric are used to compare the computational effort and accuracy of the segmented and simultaneous calibration strategies. The segmented approach is observed to yield comparable prediction uncertainty with fewer samples than simultaneous calibration for the multidisciplinary scenarios considered. The strategies are then applied to the estimation of model discrepancy in aerodynamic pressure and heat flux models using high-speed wind-tunnel data.

Nomenclature

B	=	Bayes factor
b_i^{PT}	=	ith coefficient of piston theory discrepancy model
c	=	dependence coefficient
c_i^{ERT}	=	ith coefficient of Eckert's reference temperature discrepancy model
c_p	=	specific heat at constant pressure, air
D	=	dome diameter, m
D_{KL}	=	Kullback–Leibler divergence
H	=	dome height, m
L	=	likelihood
M	=	Mach number
N	=	number of experimental observations
p	=	pressure, Pa
Q	=	aerodynamic heat flux, W/cm^2
q	=	dynamic pressure, Pa
St	=	Stanton number
T	=	temperature, K
t	=	time, s
U	=	velocity, air, m/s
w	=	panel deformation, transverse, cm
x	=	model input or chordwise spatial coordinate, m
y	=	true quantity of interest
y_D	=	data on quantity of interest
$\hat{y}$	=	model output
β	=	oblique shock angle
δ	=	model discrepancy
ε	=	measurement error
θ	=	model parameter or wedge angle
μ	=	mean
π	=	probability density function
ρ	=	correlation coefficient or density, air
σ^2	=	variance
$\boldsymbol{\Phi}$	=	set of calibration parameters

Subscripts

aw	=	adiabatic wall
D	=	observed data
p	=	pressure parameters
Q	=	heat flux parameters
w	=	wall condition
1	=	first model in a series or freestream flow conditions
2	=	second model in a series
3	=	flow at leading edge of panel
4	=	flow along panel

Superscripts

ERT	=	Eckert's reference temperature method
PT	=	piston theory
$*$	=	evaluated at the reference enthalpy

Received 16 December 2015; revision received 20 April 2016; accepted for publication 7 May 2016; published online 29 July 2016.

*Graduate Fellow, Civil and Environmental Engineering Department. Student Member AIAA.
†Research Aerospace Engineer, Air Vehicles Directorate, Structural Sciences Center. Member AIAA.
‡John R. Murray Senior Professor of Engineering, Civil and Environmental Engineering Department. Associate Fellow AIAA.

I. Introduction

MULTIDISCIPLINARY engineering problems governed by multiple physics are often analyzed by coupling several single-discipline models. For example, the predicted response of a structure subject to extreme hypersonic environments incorporates structural dynamics, heat transfer, and aerodynamics to characterize the aerothermoelastic response. The output of any individual model is subject to various sources of uncertainty: 1) natural variability in model inputs (e.g., materials and loading), 2) data uncertainty due to experimental errors and sparse data, and 3) model uncertainty due to simplified or poorly understood physics and numerical approximations [1]. Furthermore, uncertainty propagates downstream from one model to another as a function of model coupling. Model

calibration is an important step toward quantifying and reducing model uncertainty and achieving the desired level of prediction confidence.

Several model calibration methodologies exist (e.g., least squares, maximum likelihood estimation, and Bayesian estimation), and in this study, a Bayesian strategy was implemented. In Bayesian calibration, prior and posterior model parameter uncertainties can be represented as probability density functions (PDFs) [2]. Retaining uncertainty information as a PDF facilitates uncertainty quantification, model confidence assessment, and system reliability analyses [3,4]. Bayesian calibration has been implemented for model calibration in many scientific and engineering applications. Most Bayesian calibration studies have been conducted with a single model [4–7] or multiple models sharing common calibration parameters [7,8], but without interaction. The objective of this paper is to investigate strategies for Bayesian calibration of multiple interacting models that contain both local and shared parameters.

For highly coupled multiphysics problems in which data can be sparse and model parameters can be numerous [9,10], it is necessary to connect the sources of uncertainty in a systematic way. Bayesian networks are used to represent the relationships between uncertainty sources, model inputs and outputs, and data. The value of Bayesian networks lies in their ability to reduce uncertainty over the entire network based on observed data corresponding to some of the nodes. Therefore, this paper pursues a Bayesian network approach to address the challenge of calibrating several interacting models using multiple sources of data.

However, there are several challenges with Bayesian calibration of multidisciplinary models:

1) Incorporating several models into the network leads to costly likelihood functions and slow calibration convergence [11,12].

2) Often, only a subset of relevant physics is captured by a given data set [13].

3) Integrating any additional experimental data on any quantity requires recalibration simultaneously over the entire network.

The current study develops a segmented Bayesian model calibration methodology that is focused on addressing these issues by exploiting dominant connections between available data and model parameters. When applicable, the segmented calibration process partitions the parameter space and isolates individual models and their contributions to the overall uncertainty. Furthermore, segmented Bayesian calibration makes efficient use of experimental data by sequentially updating nodes in the network with relevant data, as determined by global sensitivity analysis.

One key outcome of this research is the identification of the model and data characteristics for which a segmented Bayesian calibration strategy offers the most computational benefit without compromising prediction accuracy. The characteristics considered in this research are the 1) degree of coupling, 2) relative data availability, and 3) presence of shared parameters between models. This motivates the comparison of segmented and simultaneous calibration procedures using metrics of accuracy and computational effort. The Bayes factor metric is used to compare accuracy between the competing calibration methods. The Kullback–Leibler divergence metric is used to compare convergence rates of the posterior distributions, which is indicative of the overall computational effort of performing the calibration [14].

An overview of Bayesian model calibration and Bayesian networks for multidisciplinary models is presented in Sec. II. In Sec. III, the effects of coupling, data availability, and parameter characteristics on the accuracy and computational cost of segmented calibration are investigated with two mathematical examples. An application of segmented and simultaneous calibration for a hypersonic vehicle panel subjected to aerothermal loading using wind-tunnel tests is presented in Sec. IV. Concluding remarks are provided in Sec. V, and the Appendix contains analytical derivations of calibration results from Sec. III.

II. Bayesian Model Calibration Methodology

Consider a quantity of interest y predicted by a single physics model that maps inputs $\boldsymbol{x}$ and model parameters $\boldsymbol{\theta}$ to the output $\hat{y}$, which is an inexact estimate of the true value of y. The difference between available observations y_D and the true value of y, as shown in Eq. (1), are attributed to measurement error ε_D, which is often treated as a Gaussian random variable with zero mean and unknown variance σ_D^2. To capture the disagreement between $\hat{y}$ and y due to missing physics or approximations in the model, a model discrepancy $\delta(\boldsymbol{x})$ as a function of the inputs is introduced in Eq. (2):

$$y_D = y + \varepsilon_D \tag{1}$$

$$y = \hat{y}(\boldsymbol{x};\boldsymbol{\theta}) + \delta(\boldsymbol{x}) \tag{2}$$

Input variables $\boldsymbol{x}$ are measurable quantities in laboratory or field experiments. These could be considered deterministic or stochastic with known probability distributions due to measurement errors or natural variability. In contrast to $\boldsymbol{x}$, model parameters $\boldsymbol{\theta}$ are uncertain due to lack of knowledge. Furthermore, the precise relationship between $\delta(\boldsymbol{x})$ and $\hat{y}$ as a function of $\boldsymbol{x}$ is unknown. Thus, the goal of Bayesian model calibration is to use data y_D to estimate the posterior distributions of the parameters $\boldsymbol{\theta}$, $\delta(x)$, and σ_D^2, given input–output observations and assumed prior distributions of these parameters. [In some problems, some of the unmeasured inputs may also be treated similar to calibration parameters. Epistemic uncertainty may be present regarding either deterministic inputs (i.e., unknown value) or stochastic inputs (i.e., unknown distribution type and/or parameters). In this paper, we do not explicitly consider epistemic uncertainty regarding the inputs because its treatment is similar to model parameters $\boldsymbol{\theta}$.] For a single computational model, Fig. 1 shows the Bayesian network corresponding to Eqs. (1) and (2). Bayesian calibration is an inverse problem, which is achieved by passing the information upstream from the data nodes (solid squares) to the calibration quantities (dashed circles).

Bayesian model calibration for continuous variables is performed using the Bayes formula shown in Eq. (3). The posterior probability density of the calibration quantities $\Phi = [\boldsymbol{\theta}, \delta(x), \sigma_D^2]$ is proportional to the product of the joint likelihood $L(\boldsymbol{\Phi})$ and the prior probability density $\pi(\boldsymbol{\Phi})$. Here, $\pi(\bullet)$ denotes a PDF and $\pi(\boldsymbol{\Phi}|y_D)$ refers to the updated PDF (i.e., posterior) of parameters $\boldsymbol{\Phi}$ after observing y_D.

$$\pi(\boldsymbol{\Phi}|y_D) = \frac{L(\boldsymbol{\Phi})\pi(\boldsymbol{\Phi})}{\int L(\boldsymbol{\Phi})\pi(\boldsymbol{\Phi})\,\mathrm{d}\boldsymbol{\Phi}} \propto L(\boldsymbol{\Phi})\pi(\boldsymbol{\Phi}) \tag{3}$$

Given N independent observations of y_D, the joint likelihood function of parameters $\boldsymbol{\Phi}$ is shown in Eq. (4). The likelihood is proportional to the product of joint conditional probabilities of observing y_D given a particular value of $\boldsymbol{\Phi}$:

$$L(\boldsymbol{\Phi}) \propto \prod_{i=1}^{N} \pi(y_{D,i}|\boldsymbol{\Phi}) \propto \pi(y_D|\boldsymbol{\Phi}) \tag{4}$$

The integral in the denominator of Eq. (3) simply normalizes the posterior distribution to a valid PDF, however, numerical integration schemes quickly become intractable with increasing dimension of $\boldsymbol{\Phi}$ [15]. For this reason, Bayesian calibration is often performed using Markov chain Monte Carlo (MCMC) sampling algorithms (such as Metropolis–Hastings [16], Gibbs [17], or slice sampling [18]), which make direct use of the proportionality between the numerator

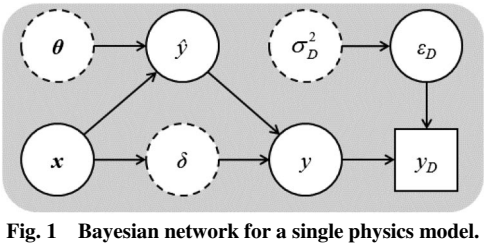

Fig. 1 Bayesian network for a single physics model.

$L(\mathbf{\Phi})\pi(\mathbf{\Phi})$ and the posterior from which to generate samples. Slice sampling is used in this paper. The computation of the likelihood function can be demanding when costly models are executed in the likelihood function. These challenges are discussed further in the next section in the context of multidisciplinary Bayesian model calibration when one or more models may be computationally prohibitive.

A. Simultaneous Bayesian Model Calibration

Consider two physical model predictions $\hat{y}_1(\boldsymbol{x};\boldsymbol{\theta}_1,\boldsymbol{\theta}_{12})$ and $\hat{y}_2(\boldsymbol{x},y_1;\boldsymbol{\theta}_2,\boldsymbol{\theta}_{12})$, which are estimates of y_1 and y_2, respectively. Each model contains inputs $\boldsymbol{x}$, uncertain model parameters $\boldsymbol{\theta}_i$, and input-dependent discrepancy functions $\delta_i(\boldsymbol{x},y_{i-1})$. There are additional uncertain parameters common to both models represented by $\boldsymbol{\theta}_{12}$. Similar to Eq. (1), the mathematical relationships observations for a two-discipline system are defined in terms of model outputs, uncertain parameters, and model discrepancy in Eqs. (5) and (6):

$$y_{D1} = y_1 + \varepsilon_{D1} = \hat{y}_1(\boldsymbol{x};\boldsymbol{\theta}_1,\boldsymbol{\theta}_{12}) + \delta_1(\boldsymbol{x}) + \varepsilon_{D1} \tag{5}$$

$$y_{D2} = y_2 + \varepsilon_{D2} = \hat{y}_2(\boldsymbol{x},y_1;\boldsymbol{\theta}_2,\boldsymbol{\theta}_{12}) + \delta_2(\boldsymbol{x},y_1) + \varepsilon_{D2} \tag{6}$$

The Bayesian network for the quantities represented by Eqs. (5) and (6) is shown in Fig. 2. The systematic organization of information in the Bayesian networks makes them ideal for multidisciplinary problems with several interacting models and limited data. For example, the connections between the two models are provided by inputs $\boldsymbol{x}$, parameters $\boldsymbol{\theta}_{12}$, and true output y_1 that feeds into $\hat{y}_2$. These relationships can be exploited such that the data furthest downstream (i.e., y_{D2}) can inform the uncertain parameters associated with both y_1 and y_2, including shared parameters $\boldsymbol{\theta}_{12}$. The influence of this downstream data depends on the relative amount of data available for y_{D1} and y_{D2}, as well as the dependence (i.e., sensitivity) of model $\hat{y}_2$ on y_1.

Given N_1 independent observations of y_{D1} and N_2 independent observations of y_{D2} for an input $\boldsymbol{x}$, the simultaneous joint likelihood function of parameters $\mathbf{\Phi} = [\boldsymbol{\theta}_1,\boldsymbol{\theta}_2,\boldsymbol{\theta}_{12},\delta_1(\boldsymbol{x}),\delta_2(\boldsymbol{x},y_1),\sigma_{D1},\sigma_{D2}]$ is shown in Eq. (7). Assuming that the observations of y_{D1} and y_{D2} are independent of each other, Eq. (7) is further divided into two separable likelihoods each corresponding to a given data set:

$$L(\mathbf{\Phi}) \propto \pi(y_{D1},y_{D2}|\mathbf{\Phi}) \quad \propto \pi(y_{D1}|\mathbf{\Phi})\pi(y_{D2}|\mathbf{\Phi}) \tag{7}$$

The likelihood in Eq. (7) requires evaluating both models $\hat{y}_1$ and $\hat{y}_2$ at every input condition to generate a single posterior sample. Additionally, the number of samples required for convergence to the posterior distribution increases with the number of calibration parameters. This computational burden motivates the investigation of more efficient calibration techniques for multidisciplinary models.

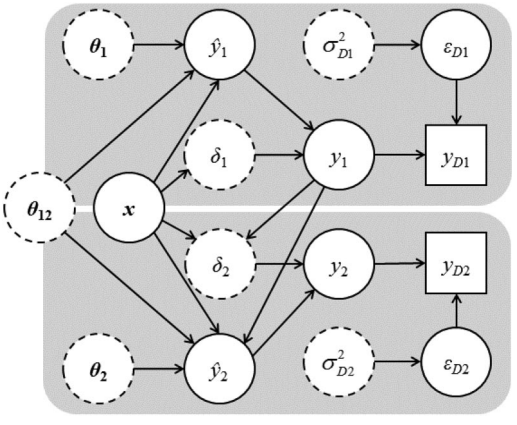

Fig. 2 Bayesian network for two-discipline system.

Therefore, in the following section, a segmented calibration method is developed to reduce the overall calibration effort.

B. Segmented Bayesian Model Calibration

The goal of segmented calibration is to isolate important relationships in the multidisciplinary Bayesian network, as well as make the best use of limited data and computational resources. In reference to the Bayesian network in Fig. 2, this leads to the parameter sets $\mathbf{\Phi}_1 = [\boldsymbol{\theta}_1,\delta_1(\boldsymbol{x}),\sigma_{D1}]$, $\mathbf{\Phi}_2 = [\boldsymbol{\theta}_2,\delta_2(\boldsymbol{x},y_1),\sigma_{D2}]$, and $\mathbf{\Phi}_{12} = \boldsymbol{\theta}_{12}$. Modifying the Bayesian framework to calibrate in a segmented manner involves the joint likelihood function in Eq. (7), which is shown in its expanded form in Eq. (8) for $\mathbf{\Phi}_1$, $\mathbf{\Phi}_2$, and $\mathbf{\Phi}_{12}$:

$$\begin{aligned} L(\mathbf{\Phi}_1,\mathbf{\Phi}_2,\mathbf{\Phi}_{12}) &\propto \pi(y_{D1}|\mathbf{\Phi}_1,\mathbf{\Phi}_2,\mathbf{\Phi}_{12})\pi(y_{D2}|\mathbf{\Phi}_1,\mathbf{\Phi}_2,\mathbf{\Phi}_{12}) \\ &\propto \pi(y_{D1}|\mathbf{\Phi}_1,\mathbf{\Phi}_{12})\pi(y_{D2}|\mathbf{\Phi}_1,\mathbf{\Phi}_2,\mathbf{\Phi}_{12}) \\ &\approx \pi(y_{D1}|\mathbf{\Phi}_1,\mathbf{\Phi}_{12})\pi(y_{D2}|\mathbf{\Phi}_{1|D1},\mathbf{\Phi}_2,\mathbf{\Phi}_{12}) \end{aligned} \tag{8}$$

Because parameters $\mathbf{\Phi}_2$ are not connected to y_{D1} in the Bayesian network, the first likelihood in the first step of Eq. (8) can exclude $\mathbf{\Phi}_2$ while still being equivalent to Eq. (7), as shown in the second step. The mechanism of segmenting the likelihood is shown between the second and last step of Eq. (8). The approximation sign implies that, in the segmented approach, the quantity $\pi(y_{D1}|\mathbf{\Phi}_1,\mathbf{\Phi}_{12})\pi(y_{D1}|\mathbf{\Phi}_1,\mathbf{\Phi}_2,\mathbf{\Phi}_{12})$ is approximated by $\pi(y_{D1}|\mathbf{\Phi}_1,\mathbf{\Phi}_{12})\pi(y_{D1}|\mathbf{\Phi}_{1|D1},\mathbf{\Phi}_2,\mathbf{\Phi}_{12})$, in which $\mathbf{\Phi}_{1|D1}$ denotes the posteriors of $\mathbf{\Phi}_1$ from the first calibration. The validity of this approximation is verified in Sec. II.C with a global sensitivity analysis.

With a segmented likelihood in Eq. (8), two Bayesian posteriors emerge: one using the likelihood defined by y_{D1} in Eq. (9) and another using the likelihood defined by y_{D2} and conditioned on $\mathbf{\Phi}_{1|D1}$ in Eq. (10):

$$\pi(\mathbf{\Phi}_1,\mathbf{\Phi}_{12}|y_{D1}) \propto \pi(y_{D1}|\mathbf{\Phi}_1,\mathbf{\Phi}_{12})\pi(\mathbf{\Phi}_1,\mathbf{\Phi}_{12}) \tag{9}$$

$$\begin{aligned} \pi(\mathbf{\Phi}_2,\mathbf{\Phi}_{12}|y_{D2}) &\propto \pi(y_{D2}|\mathbf{\Phi}_{1|D1},\mathbf{\Phi}_2,\mathbf{\Phi}_{12})\pi(\mathbf{\Phi}_2,\mathbf{\Phi}_{12|D1}) \\ &\propto \pi(y_{D2}|\mathbf{\Phi}_{1|D1},\mathbf{\Phi}_2,\mathbf{\Phi}_{12})\pi(\mathbf{\Phi}_2)\pi(\mathbf{\Phi}_{12|D1}) \end{aligned} \tag{10}$$

The shared parameters $\mathbf{\Phi}_{12}$ are updated in both calibration segments where the posterior PDF of $\mathbf{\Phi}_{12|D1}$ from the first calibration becomes the prior of the second and assumed to be independent of $\mathbf{\Phi}_2$, as shown in Eq. (10). In some cases, parameters in $\mathbf{\Phi}_{12}$ can be included solely in the first or second calibration, if a sensitivity analysis determines one particular model is more sensitive to those parameters. A quantitative sensitivity analysis on all outputs of interest presented in the next section helps determine an appropriate calibration strategy (i.e., segmented or simultaneous) for a given multidisciplinary system.

C. Global Sensitivity Analysis

To justify a segmented model calibration strategy, the models and parameters need to satisfy these three conditions:

1) $\mathbf{\Phi}_1$ should have low sensitivity to data on y_{D2}.

2) The sensitivity of model $\hat{y}_2$ to $\mathbf{\Phi}_2$ should be greater than to $\mathbf{\Phi}_1$. This occurs when there is little to no dependence between models (i.e., weak coupling).

3) The output $\hat{y}_1$ should be insensitive to $\mathbf{\Phi}_2$, which is always true for strictly feedforward models.

A sensitivity analysis is used to validate these three conditions, as well as identify the sources of uncertainty that contribute significantly to the total uncertainty in each multidisciplinary model output.

In contrast to gradient-based local sensitivities at a chosen nominal value, a global sensitivity analysis uses parameter probability information and quantifies both the individual and interactive effects of the various uncertainty sources on the model output uncertainty. This is especially important in a multidisciplinary model calibration in which many uncertain and interrelated parameters are present [19].

Based on the variance decomposition theorem stated in Eq. (11), the overall variance in a model output $\hat{y}$ can be decomposed into 1) the variance of the expectation of $\hat{y}$ conditioned on a fixed input θ^i with all other inputs (θ^{-i}) allowed to vary, and 2) the expectation of the variance of $\hat{y}$ conditioned on the same set [20,21]:

$$\mathrm{Var}(\hat{y}) = \mathrm{Var}_{\theta^i}[E_{\theta^{-i}}(\hat{y}|\theta^i)] + E_{\theta^i}[\mathrm{Var}_{\theta^{-i}}(\hat{y}|\theta^i)] \tag{11}$$

There are two quantities to consider in global sensitivity analysis: the first-order effects and the total effects of θ^i. The first-order effects index quantifies the individual contribution of θ^i to variance in the output $\hat{y}$ and is given as

$$S^i_{1,y} = \frac{\mathrm{Var}_{\theta^i}[E_{\theta^{-i}}(\hat{y}|\theta^i)]}{\mathrm{Var}(\hat{y})} \tag{12}$$

In Eq. (12), the denominator $\mathrm{Var}(\hat{y})$ is the total variance of a model output $\hat{y}$ considering uncertainty in all parameters $\boldsymbol{\theta}$. In addition to individual contribution, a parameter may contribute additional uncertainty in the output through interactions with other parameters. The total effects index considers the interactions between the ith parameter and all other parameters and is essential to make informed decisions regarding calibration. The total effects index is given in Eq. (13):

$$S^i_{T,y} = 1 - \frac{\mathrm{Var}_{\theta^{-i}}[E_{\theta^i}(\hat{y}|\theta^{-i})]}{\mathrm{Var}(\hat{y})} \tag{13}$$

Parameter sensitivities can also be grouped together to compute of the sensitivity of output $\hat{y}_2$ to groups of parameters $\boldsymbol{\Phi}_1$, $\boldsymbol{\Phi}_2$, and $\boldsymbol{\Phi}_{12}$ [21]. The sum of these sensitivities should be less than or equal to unity, and their relative importance to $\hat{y}_2$ can be used to decide the applicability of a segmented calibration strategy. The analytical example in Sec. III analyzes the sensitivity of $\hat{y}_2$ to $\boldsymbol{\Phi}_1$ and the performance of segmented calibration.

D. Metrics for Comparison of Segmented and Simultaneous Calibration Strategies

1. *Likelihood Ratio*

As a measure of how accurate the segmented calibration strategy is compared with the simultaneous calibration strategy, a likelihood ratio of the two posterior distributions of parameters obtained from segmented and simultaneous calibration given observed data is computed using Eq. (14). The likelihood ratio compares the support of the data to the null hypothesis (i.e., model output with segmented calibrated parameters $\boldsymbol{\Phi}_{\mathrm{seg}}$ with joint PDF π_{seg} is equal to the observed data) vs the alternate hypothesis (i.e., model output with parameters calibrated simultaneously $\boldsymbol{\Phi}_{\mathrm{sim}}$ with joint PDF π_{sim} is equal to the observed data) [22]. Assuming the observed data sets y_{D1} and y_{D2} are independent, the joint likelihood is equivalent to the product of the individual likelihoods from each set of data:

$$\begin{aligned} B &= \frac{\int \pi(y_{D1}, y_{D2}|\boldsymbol{\Phi}_{\mathrm{seg}})\pi(\boldsymbol{\Phi}_{\mathrm{seg}})\,\mathrm{d}\boldsymbol{\Phi}_{\mathrm{seg}}}{\int \pi(y_{D1}, y_{D2}|\boldsymbol{\Phi}_{\mathrm{sim}})\pi(\boldsymbol{\Phi}_{\mathrm{sim}})\,\mathrm{d}\boldsymbol{\Phi}_{\mathrm{sim}}} \\ &= \frac{\int \pi(y_{D1}|\boldsymbol{\Phi}_{\mathrm{seg}})\pi(y_{D2}|\boldsymbol{\Phi}_{\mathrm{seg}})\pi(\boldsymbol{\Phi}_{\mathrm{seg}})\,\mathrm{d}\boldsymbol{\Phi}_{\mathrm{seg}}}{\int \pi(y_{D1}|\boldsymbol{\Phi}_{\mathrm{sim}})\pi(y_{D2}|\boldsymbol{\Phi}_{\mathrm{sim}})\pi(\boldsymbol{\Phi}_{\mathrm{sim}})\,\mathrm{d}\boldsymbol{\Phi}_{\mathrm{sim}}} \end{aligned} \tag{14}$$

The preceding ratio is the integrated likelihood ratio (i.e., it is evaluated over all possible values of the posterior parameters); this integrated likelihood ratio is referred to as the Bayes factor [23,24]. Effectively, the Bayes factor is a direct comparison between the segmented likelihood in Eq. (8) and the simultaneous likelihood in Eq. (7). Thus, $B > 1$ indicates larger support for the numerator.

2. *Kullback–Leibler Divergence*

Computational effort is compared using the posterior convergence rates from both segmented and simultaneous calibration strategies, which can be computed using the Kullback–Leibler (K-L) divergence measure presented in Eq. (15) [14]. The K-L divergence is an indicator of similarity between PDFs, and so a smaller value of K-L divergence indicates a smaller dissimilarity between them. In this paper, the distributions of interest are the posterior distributions obtained from the calibration after the ith MCMC sample (slice sampling was used here, but other MCMC methods could also be used) $\pi_i(\boldsymbol{\Phi})$ and the posterior distributions after $i+1$ samples $\pi_{i+1}(\boldsymbol{\Phi})$. The K-L divergence integral in Eq. (15) can be computed using Monte Carlo integration with the samples generated from the sampling algorithm (e.g., slice sampling):

$$D_{\mathrm{KL}}(\pi_i||\pi_{i+1}) = \int \pi_i(\boldsymbol{\Phi})\,\log\frac{\pi_i(\boldsymbol{\Phi})}{\pi_{i+1}(\boldsymbol{\Phi})}\,\mathrm{d}\boldsymbol{\Phi} \geq 0 \tag{15}$$

Therefore, a simultaneous calibration strategy will track one K-L divergence of the posterior PDF of $\boldsymbol{\Phi}$ until convergence is reached. In contrast, a segmented calibration strategy monitors the K-L divergence of each calibration subset. For the analytical example in Sec. III and the hypersonic application problem in Sec. IV, two calibration segments are used.

III. Mathematical Examples

In this section, Bayesian multimodel calibration is first investigated for a mathematical example in which analytical posteriors are obtainable. The derivations of the posterior PDFs for the analytical example using conjugate distributions are given in the Appendix. Second, an empirical example that has shared inputs x and parameter θ_{12} is explored.

First, consider two models $y_1 = \theta_1$ and $y_2 = cy_1 + \theta_2$ that are related through a dependence coefficient c. Parameters θ_1 and θ_2 are uncertain and are to be calibrated using observations y_{D1} and y_{D2} on outputs y_1 and y_2, respectively. Here, model discrepancy is assumed not to be present so that $y_1 = \hat{y}_1$ and $y_2 = \hat{y}_2$, as shown in Eqs. (16) and (17). The observations y_{D1} and y_{D2} contain measurement errors, assumed to be Gaussian with zero mean and known variances σ^2_{D1} and σ^2_{D2}, respectively:

$$y_{D1} = y_1 + N(0, \sigma_{D1}) = \theta_1 + N(0, \sigma_{D1}) \tag{16}$$

$$y_{D2} = y_2 + N(0, \sigma_{D2}) = cy_1 + \theta_2 + N(0, \sigma_{D2}) \tag{17}$$

The Bayesian network for this system is shown in Fig. 3, in which the two models are connected via nodes y_1 and y_2. The strength of their dependence is dictated by c, which influences the viability of a segmented Bayesian calibration strategy for the two models.

In Sec. III.A, prior distributions are selected for θ_1 and θ_2 and used to discuss the effect of model dependence on model output sensitivities. The posterior PDFs and variance ratios between the segmented and simultaneous methodologies are derived in Sec. III.B, and their accuracy is compared analytically in Sec. III.C. The calibrations are performed numerically in Sec. III.D using slice sampling and computational effort is assessed using K-L divergence.

A. Model Dependence and Prior Sensitivities

Conjugate distributions facilitate the derivation of the segmented and simultaneous posteriors, where, for simplified problems, the distribution type of the posterior is the same as that of the prior when combined with an appropriate choice of the likelihood function (e.g.,

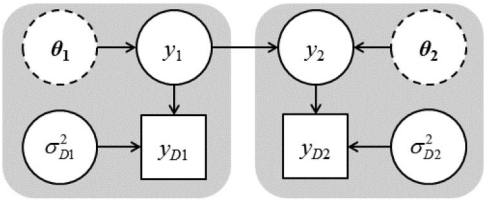

Fig. 3 Bayesian network for mathematical example.

Table 1 True parameter values, prior means and variances, and measurement error variance

Quantity	Value
Parameter θ_1	
Truth	1.2
$\mu_{\theta 1}$	1.3
$\sigma^2_{\theta 1}$	1.0e-2
Parameter θ_2	
Truth	0.9
$\mu_{\theta 2}$	0.7
$\sigma^2_{\theta 2}$	1.0e-2
Measurement error variance	
σ^2_{D1}	2.5e-3
σ^2_{D2}	10.0e-3

a normal likelihood function and normal prior result in a normal posterior) [25]. For this reason, it is convenient to exploit the simple linear relationship between Eqs. (13) and (14) and derive the posterior statistics for θ_1 and θ_2 using normal priors $\pi(\theta_1) \sim N(\mu_{\theta 1}, \sigma_{\theta 1})$ and $\pi(\theta_2) \sim N(\mu_{\theta 2}, \sigma_{\theta 2})$ given in Table 1. In addition, there are N_1 observations of y_{D1} and N_2 observations of y_{D2} with known observation variances σ^2_{D1} and σ^2_{D2} also given in Table 1.

The prior first-order sensitivities of model y_2 to the uncertainty in θ_1 and θ_2 for dependence coefficients of $c = [0, 5]$ are computed using Eqs. (18) and (19), and are presented in Fig. 4. They represent the contribution to the total variance in y_2 from each source of uncertainty. Because the priors are assumed uncorrelated, their first-order and total effects are equivalent. Furthermore, due to the strictly feedforward nature of the models, the sensitivity of y_1 to θ_1 is one and its sensitivity to θ_2 is zero:

$$S^{\theta 1}_{1,y2} = S^{\theta 1}_{T,y2} = \frac{\mathrm{Var}_{\theta 1}(E_{\theta 1}(y_2|\theta_2))}{\mathrm{Var}(y_2)} = \frac{c^2\sigma^2_{\theta 1}}{c^2\sigma^2_{\theta 1} + \sigma^2_{\theta 2}} \tag{18}$$

$$S^{\theta 2}_{1,y2} = S^{\theta 2}_{T,y2} = \frac{\mathrm{Var}_{\theta 2}(E_{\theta 2}(y_2|\theta_1))}{\mathrm{Var}(y_2)} = \frac{\sigma^2_{\theta 2}}{c^2\sigma^2_{\theta 1} + \sigma^2_{\theta 2}} \tag{19}$$

At $c = 0$, parameter θ_1 has no influence on output y_2, as indicated in Fig. 4, with zero sensitivity. Intuitively, increasing the dependence coefficient results in increased sensitivity of y_2 to the uncertainty in θ_1 and asymptotically approaches one as c increases. Note that, at $c = 1$, the first-order sensitivities are 0.5 for both θ_1 and θ_2 because the variance contributions from $c\theta_1$ and θ_2 on output y_2 are equal.

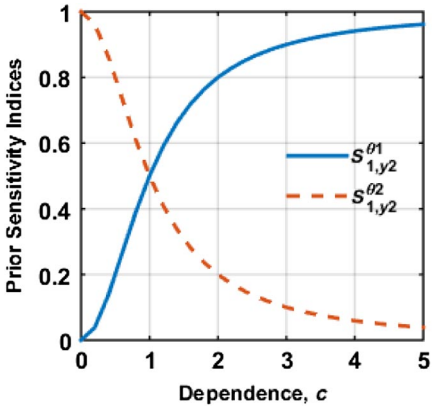

Fig. 4 Prior sensitivity of model output y_2 to uncertainty in θ_1 and θ_2.

B. Calibration Results for Analytical Example

The posterior distributions for segmented and simultaneous calibrations are derived in the Appendix and used to test the effects of the dependence coefficient c and the relative number of data points N_1 and N_2 on the posterior parameter and prediction uncertainty. The variances of θ_1 from a segmented strategy [Eq. (A4)] and from a simultaneous strategy [Eq. (A22)] as a function of N_1 are shown in Fig. 5 for two cases of downstream data: $N_2 = 5$ and $N_2 = 50$.

It is observed in Fig. 5 that the segmented calibration of θ_1 is solely dependent on the amount of data on y_1 and is unaffected by the amount of data on y_2 or the dependence coefficient. In contrast, a simultaneous strategy does allow downstream information y_{D2} to influence θ_1 noticeably at low levels of N_1 and large c. These figures imply that, as model dependence increases, downstream data become important and a segmented calibration strategy fails to benefit from this information. However, the effectiveness of these downstream data is limited. For example, when $c = 5$ the amount of uncertainty reduction in θ_1 between $N_2 = 5$ and $N_2 = 50$ for a simultaneous strategy is only 8.8%.

In contrast to the posterior variances of θ_1, Fig. 6 shows the posterior variances of θ_2 computed using Eqs. (A8) and (A16) in the Appendix. When there is ample upstream data (i.e., $N_1 = 50$), the posterior variance from the segmented strategy is effectively independent of c. This means that θ_1 does not influence the downstream segmented calibration when it is well characterized. However, when $N_1 = 5$, more uncertainty propagates forward, leading to more uncertainty in θ_2. In a simultaneous strategy, however, the correlations between θ_1 and θ_2 posterior samples [denoted by $\rho(\theta_1, \theta_2)$], are negative and lead to observing more uncertainty in θ_2 compared with the segmented strategy. Conversely, the correlations $\rho(\theta_1, \theta_2)$ in a segmented strategy are zero.

As shown in Fig. 7, the simultaneous calibration correlation coefficient in Eq. (A26) is dependent on relative data sizes corresponding to the two model outputs. The parameters exhibit strong negative correlations when N_1 is limited and with increased model dependence.

To account for $\rho(\theta_1, \theta_2)$, posterior variances in y_2 for both segmented and simultaneous strategies for the analytical example are given in Eq. (20) and shown in Fig. 8. Even though the variance of θ_2 from simultaneous calibration with $N_1 = 5$ is significantly greater than the variance segmented calibration of θ_2, neglecting the negative correlation between θ_1 and θ_2 in a segmented strategy results in more uncertainty propagating downstream to y_2. In other words, neglecting the correlation results in greater downstream prediction uncertainty from the segmented calibration strategy as the dependence between the models increases:

$$\mathrm{var}(y_2) = c^2\mathrm{var}(\theta_1) + \mathrm{var}(\theta_2) + 2c\rho(\theta_1, \theta_2)\sigma_{\theta 1}\sigma_{\theta 2} \tag{20}$$

C. Comparison of Segmented and Simultaneous Calibration Results

The posterior distributions resulting from the segmented and simultaneous calibration strategies can be compared using several different metrics. Here, we compare their mean values and variances; the former is related to bias and the latter to precision. The mean values from both strategies were found to be identical; thus, there is no bias introduced by the segmented strategy. Figure 9 shows the variance ratio for the posterior distributions of θ_1, θ_2, and y_2, with the variance from the simultaneous calibration as the denominator and the variance from the segmented calibration as the numerator. Therefore, a variance ratio greater than one indicates that the result of the segmented strategy contains more uncertainty (i.e., more imprecision). Figure 9 shows these ratios for the four data scenarios mentioned earlier.

The variance ratios in Fig. 9 continue to suggest that limited upstream data impede the performance of a segmented calibration. First, the variance ratio for $y_1 = \theta_1$ prediction (which is an increasing function of c) shows significant increase when $N_1 = 5$ (because the simultaneous strategy uses y_{D2} data to reduce the variance of θ_1). This

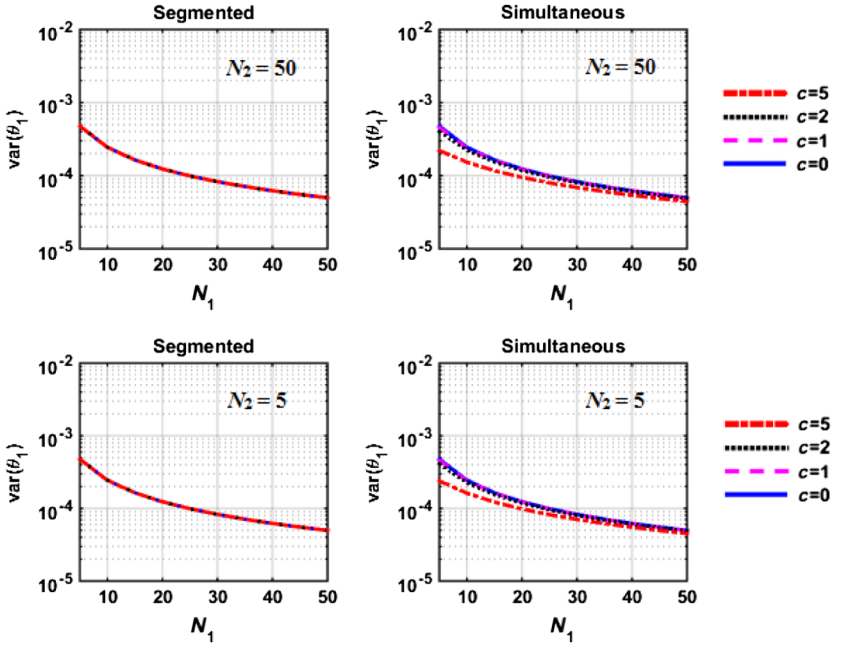

Fig. 5 Posterior variance of θ_1 as a function of data on y_1.

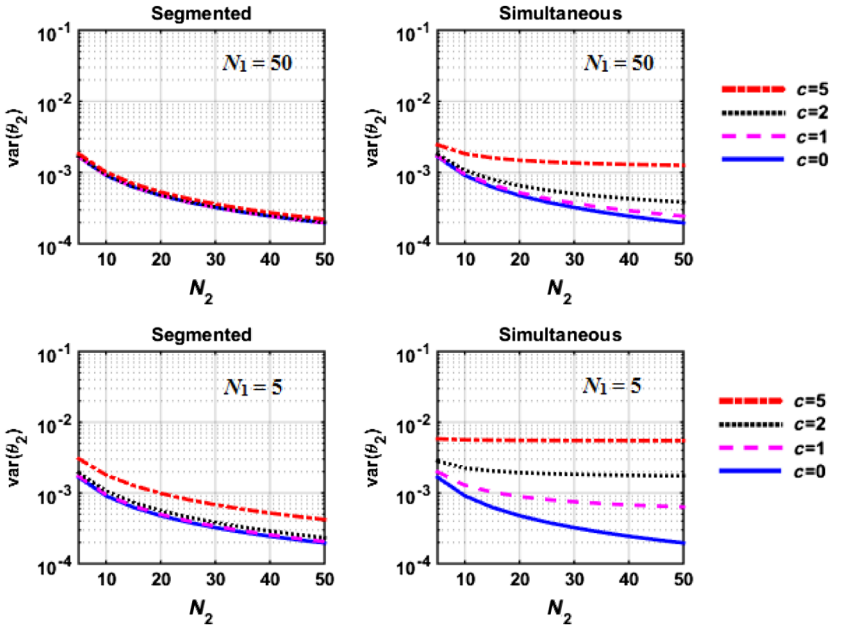

Fig. 6 Posterior variance of θ_2 as a function of data on y_2.

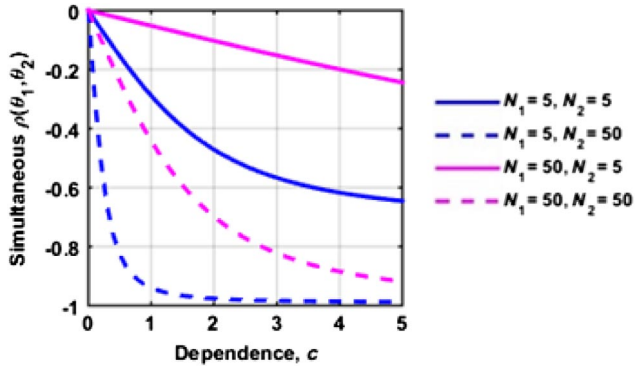

Fig. 7 Posterior correlation between θ_1 and θ_2 as a function of c (computed using simultaneous calibration).

effect of limited data on y_{D1} is worsened in downstream predictions in a segmented calibration strategy, as seen from the increasing variance ratio for y_2. Regarding θ_2, the variance ratio for $N_1 = 5$ and $N_2 = 50$ is significantly less than one because all of the y_{D2} data are used for the posterior estimation of θ_2 (thus reducing its variance) in the segmented calibration, whereas in the simultaneous strategy, the y_{D2} data are used to estimate the posteriors of both θ_1 and θ_2 (resulting in less variance reduction of θ_2). However, ignoring the negative correlation between θ_1 and θ_2 means more uncertainty is propagating downstream to y_2 in a segmented calibration strategy, resulting in a larger variance ratio for y_2.

D. Comparison of Computational Effort

The Kullback–Leibler divergence integral in Eq. (15) was computed numerically using Monte Carlo integration with the 10^4 posterior slice samples generated from calibration. A smaller D_{KL} at a given posterior sample i means that the two posterior distributions

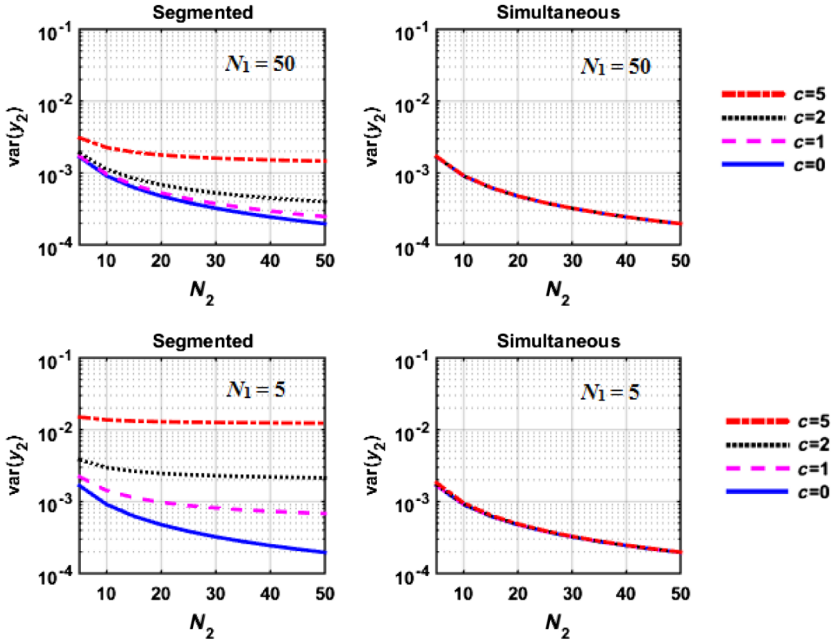

Fig. 8 Posterior variance of y_2 as a function of data on y_2.

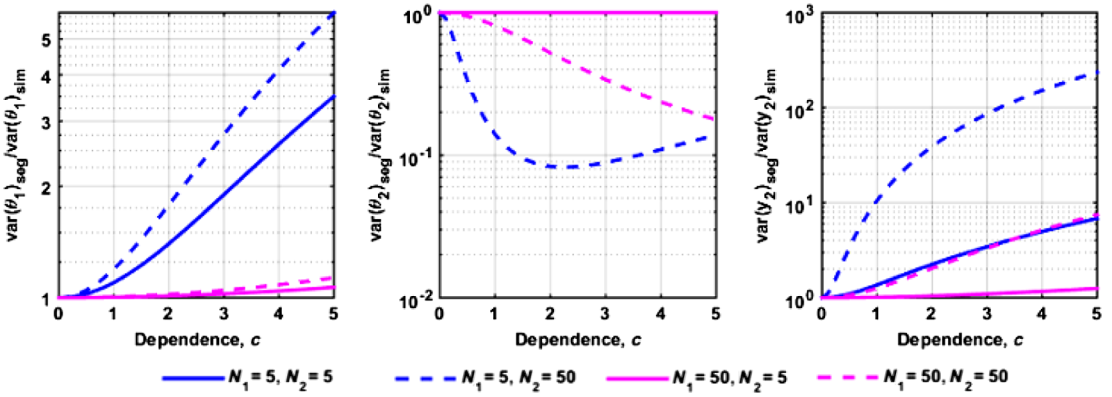

Fig. 9 Variance ratios for θ_1, θ_2, and y_2 predictions from segmented and simultaneous calibration.

defined by the samples up to i and up to $i-1$ are more similar, hence, the distribution is converging at a faster rate. It is observed that the convergence rate is not affected by the amount of data. Consider the convergence rates for $N_1 = 50$ and $N_2 = 50$ for a dependence coefficient of 2 shown in Fig. 10. Here, convergence is assumed to be reached when $\log(D_{\mathrm{KL}}) = -10$.

From Fig. 10, it can be seen that both segmented calibrations (the first using y_{D1} to calibrate θ_1 and the second using y_{D2} to calibrate θ_2) achieve a smaller K-L divergence than the simultaneous calibration strategy. Both segmented calibrations reached convergence in approximately 2500 samples from each model, whereas the simultaneous converged in approximately 4500 samples from each model. This resulted in a computational savings of 2000 (45%) individual $\hat{y}_1$ simulations and 2000 (45%) $\hat{y}_2$ simulations using a segmented calibration strategy. With costly model simulations typical of multidisciplinary analyses, these percentages can significantly influence computation time.

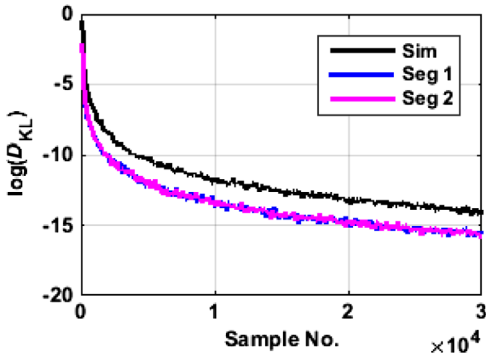

Fig. 10 Kullback–Leibler divergence for segmented and simultaneous calibration.

E. Extension: Shared Inputs and Parameters

Building on the analytical example in Eqs. (16) and (17) to more closely resemble the Bayesian network in Fig. 2, consider the addition of shared input x and parameter θ_{12}. Thus, the preceding mathematical example is extended further, as shown in Eqs. (21) and (22). Note that we still do not include model discrepancy terms, because those would be calibrated similar to local parameters θ_1 and θ_2. However, model discrepancy terms are explicitly considered in Sec. IV with aerothermal model errors:

$$y_{D1} = \theta_1 + \theta_{12}x + N(0, \sigma_{D1}) \tag{21}$$

$$y_{D2} = cy_1 + \theta_2 + \theta_{12}x^2 + N(0, \sigma_{D2}) \tag{22}$$

Data were synthetically generated for this problem using the true values of θ_1 and θ_2 and known variances σ_{D1}^2 and σ_{D2}^2 from Table 1

Table 2 True parameter values, prior mean, and variance of θ_{12}

Quantity	Value
Parameter θ_{12}	
Truth	0.5
$\mu_{\theta 2}$	0.5
$\sigma^2_{\theta 2}$	1.0e-2

along with the true value of θ_{12} shown in Table 2. For the data cases considered (i.e., $N_1 = 5$, $N_1 = 50$, $N_2 = 5$, $N_2 = 50$), random realizations of y_{D1} and y_{D2} were generated at equidistant points between zero and one. For example, when $N_1 = 5$, one random realization of y_{D1} at each $x = [0, 0.25, 0.5, 0.75, 1]$ was used for calibration.

Because an analytical calibration solution was not available, slice sampling was used to generate 20,000 posterior samples of θ_1, θ_{12}, and θ_2 from both segmented and simultaneous calibration strategies. The calibrated model predictions extrapolated to $x = 2$ compared with the data are shown in Fig. 11 for the particular case when $c = 5$, $N_1 = 5$, and $N_1 = 50$. (Note that the analytical example in Secs. III.A–III.D demonstrated that the largest sacrifice in downstream prediction accuracy from a segmented calibration strategy occurred when the dependence coefficient was large and data on the first model were low.) Accuracy comparisons using the Bayes factor will be made between the two calibration strategies using the known true values of y_1 and y_2 at an extrapolation point $x = 1.25$.

The posterior predictions in Fig. 11 demonstrate how the extrapolation confidence in a segmented strategy is affected by the amount of upstream data available. First, the prediction of y_1 based on segmented calibration contains more uncertainty and bias than that based on simultaneous calibration, indicated by the wider confidence ("Conf.") bounds in Fig. 11. For example, at $x = 1.25$ ("Validation Pt."), the variance ratio between the predictions of y_1 from the two strategies is observed to be 5.9 (i.e., segmented vs simultaneous) and the variance ratio for y_2 is observed to be 33.3. These trends are similar to the previous example.

Figure 12 shows the prior and posterior distributions from the segmented and simultaneous calibration strategies compared with the true parameter values of θ_1, θ_{12}, and θ_2. The prior distribution parameters ("prior") and true values ("true") are taken from Tables 1 and 2.

The results show that the posterior distribution of θ_1 from both calibration methods contains positive bias relative to the true value of θ_1. For segmented calibration, this positive bias in θ_1 from the first calibration ("Seg 1") is accounted for in the second calibration ("Seg 2") with negative bias in θ_2 due to their relationship in Eq. (22). In contrast, the posterior of θ_1 in the simultaneous calibration ("Sim") has less uncertainty and bias from the use of downstream information. Similar to the analytical example, the posterior uncertainty in θ_2 from simultaneous calibration is larger than that from segmented calibration when $c = 5$ due to the insensitivity of y_2 to θ_2 at higher dependence coefficients.

Second, the two posterior distributions of θ_{12} from segmented calibration (one from each segment) are both biased. The bias in θ_{12} from the first calibration segment is from limited data $N_1 = 5$. The second calibration of θ_{12} aims to account for the previous negative bias in y_1 data by adjusting θ_{12} positively with the information on y_2.

At $x = 1.25$, Fig. 11 compares the accuracy of the calibrated models from each method for dependence coefficients ranging from zero to five, using the Bayes factors. The Bayes factors were calculated using Eq. (14), in which B_1 and B_2 correspond to y_1 and y_2, respectively. With the integrated likelihood from segmented calibration in the numerator, a Bayes factor less than one indicates that the validation data give larger support to the simultaneous prediction.

As previously seen in the analytical example, the Bayes factors in Fig. 13 indicate that the accuracy of a segmented calibration strategy on the first model prediction is primarily a function of the data available on y_1, rather than the dependence between the models. When $N_1 = 5$, the Bayes factor B_1 across all values of c averages to 0.65, and when $N_1 = 50$, they average to 0.98. Also similar to the analytical example, the Bayes factor for y_2 is a function of both the available data and the dependence coefficient and decreases as a function of c more rapidly when there is low data on the first model ($N_1 = 5$) compared with when $N_1 = 50$.

In summary, segmented calibration might be an acceptable approximation to simultaneous calibration when the level of dependence between the models is low or when ample data are available on the first model output. Further, segmented calibration ignores negative correlation between posterior parameter sets, thus propagating more uncertainty to downstream model predictions than simultaneous calibration. However, the segmented strategy was seen to offer significant computational savings. Considering the tradeoff between accuracy and computational effort, the segmented strategy appears attractive as a calibration alternative when there is ample data

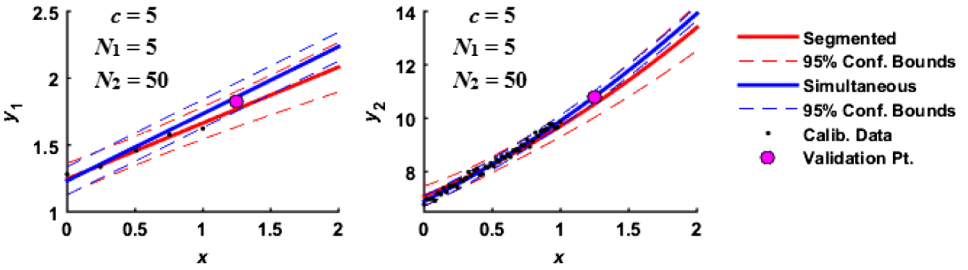

Fig. 11 Calibrated y_1 and y_2 predictions when $c = 5$, $N_1 = 5$, and $N_2 = 50$.

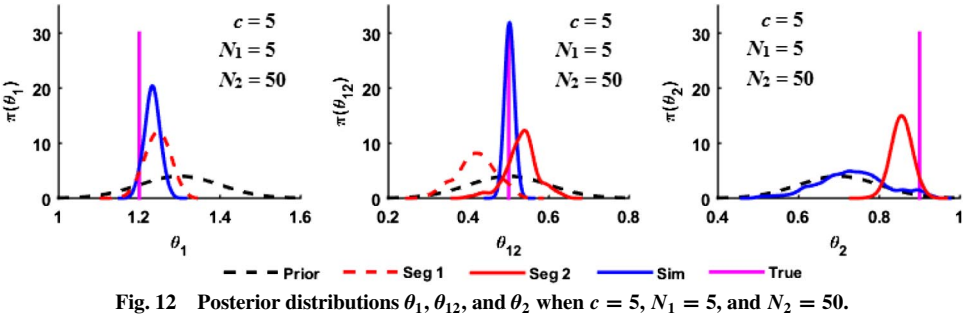

Fig. 12 Posterior distributions θ_1, θ_{12}, and θ_2 when $c = 5$, $N_1 = 5$, and $N_2 = 50$.

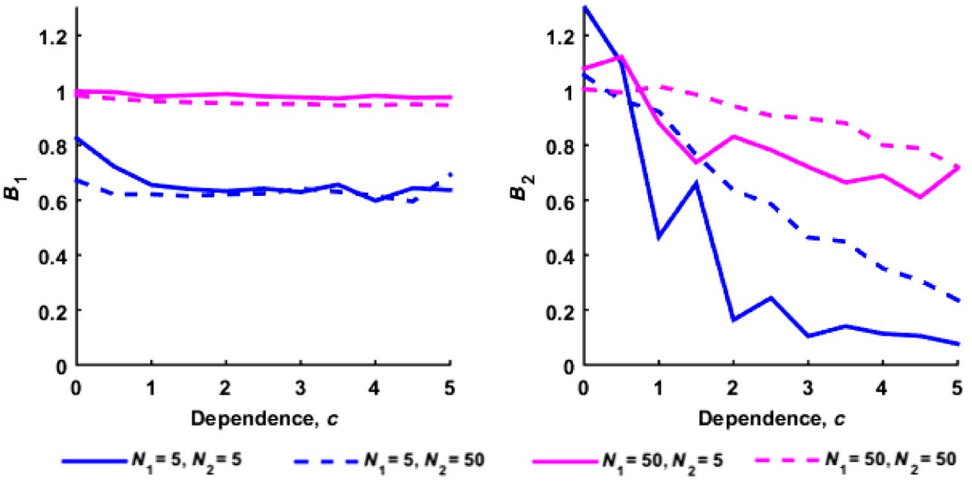

Fig. 13 Bayes factors for y_1 and y_2 predictions at $x = 1.25$ from segmented and simultaneous calibration.

on the first model or when the dependence between the two models is low.

IV. Application Problem: Aerothermal Models

The mathematical example problems presented in the preceding sections highlighted the factors that affect the calibration of multidisciplinary models, which include model dependence and relative data availability on each model output. In this section, multidisciplinary model calibration is investigated for coupled aerothermal models predicting the pressure and heating on an aircraft panel subjected to hypersonic flow conditions. The investigation focuses on whether a segmented calibration strategy is suitable for this multidisciplinary, and potentially costly, simulation.

Aircraft structures exposed to extreme environments are subjected to coupled aerodynamic, thermal, and acoustic loading [26–33]. Neglecting these interactions can lead to gross errors in model predictions [31–37]. Consider a panel on the forebody of a representative hypersonic vehicle with wedge angle θ shown in Fig. 14 [38]. As the vehicle is subjected to hypersonic flow, an attached oblique shock with angle β is created at the leading edge (location 1). This results in heating and aerodynamic pressure applied to the area of interest (location 4).

Figure 15 schematically illustrates the aerothermal interactions consisting of aerodynamic pressure and heat flux model components. Given the freestream pressure p_1, temperature T_1, Mach number M_1, and panel deformation configuration w, the local flow conditions at the panel are predicted (p_4, T_4, M_4). The aerothermal models propagate

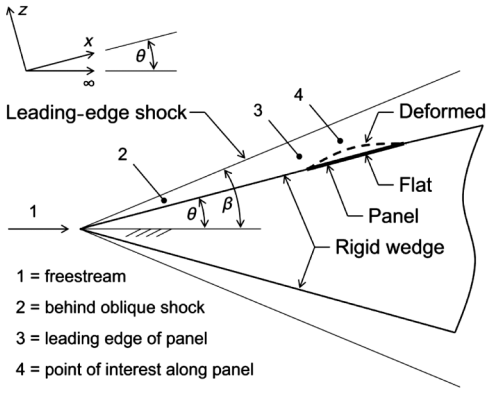

Fig. 14 Representative hypersonic vehicle and panel deformation [38].

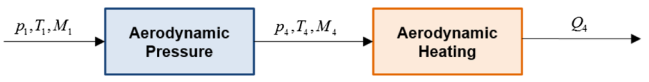

Fig. 15 Schematic of aerothermal models.

the prediction such that that the local aerodynamic pressure p_4 is used by the aeroheating model to compute the applied heat flux Q_4 on the panel. In a coupled aerothermoelastic analysis, upstream uncertainty and errors from model estimates propagate downstream, which impacts the accuracy of the overall aerothermoelastic response prediction. These errors further compound through time and motivate the need to identify and reduce uncertainty sources using sparse experimental data available for calibration.

The following subsections apply segmented and simultaneous Bayesian model calibration to an aerodynamic pressure prediction model (i.e., third-order piston theory) and heating prediction model (i.e., Eckert's reference temperature method) using available high-speed wind-tunnel tests. The Glass and Hunt [37] wind-tunnel tests, presented in Sec. IV.B, measured both pressure and heat flux on several rigid domes with different height-to-diameter ratios intended to simulate a panel deforming into the flow. This problem provides a realistic test case for segmented calibration, because both model output quantities of interest were measured, with potential tradeoffs between computational cost and model uncertainty. A comparison of the calibration strategies is quantified with Bayes factors as well as Kullback–Leibler divergence to measure the number of samples required for posterior convergence.

A. Aerothermal Models and Bayesian Network

The two models being considered in this aerothermal application problem are third-order piston theory and Eckert's reference temperature method. Piston theory (PT) provides a simplified relationship between the unsteady pressure on the panel and turbulent surface pressure [35], which is desirable for computational tractability in aerothermoelastic predictions. The leading-edge Mach number M_3 and dynamic pressure q_3 computed from oblique shock relations are used in piston theory to approximate the aerodynamic pressure load chordwise across the panel (location 4 in Fig. 11). Piston theory accounts for both the slope of the panel ($\partial w/\partial x$) and the velocity of deformation ($\partial w/\partial t$), however, because the wind-tunnel specimens considered in this study are rigid (further explained in Sec. IV.B), the time-dependent terms are removed and a third-order expansion of piston theory is written as Eq. (23):

$$p_4^{\mathrm{PT}} = p_3 + 2\frac{q_3}{M_3}\left[\frac{\partial w}{\partial x} + \frac{\gamma+1}{4}M_3\left(\frac{\partial w}{\partial x}\right)^2 + \frac{\gamma+1}{12}M_3\left(\frac{\partial w}{\partial x}\right)^3\right] \tag{23}$$

After calculating the aerodynamic pressure and flow conditions along the panel surface, the aerodynamic heat flux is predicted using the computationally efficient Eckert's reference temperature method assuming a calorically perfect gas [36]. Eckert's reference temperature is computed by Eq. (24) and the heat flux across the spherical dome is computed in Eq. (25):

$$T^* = T_3 + 0.5(T_w - T_e) + 0.22(T_{aw} - T_3) \tag{24}$$

$$Q_4^{\mathrm{ERT}} = St^* \rho^* U_e c_p^* (T_{aw} - T_w) \tag{25}$$

in which St^* is the reference Stanton number, ρ^* is the reference density, U_e is the inviscid flow velocity at the dome location, c_p^* is the reference specific heat, T_{aw} and T_w are the adiabatic wall and actual wall temperature, respectively, and T_e is the boundary-layer edge temperature.

Consistent with the Bayesian model calibration framework presented in Sec. II, the measurement noise in pressure $\varepsilon_{D,p}$ and heat flux $\varepsilon_{D,Q}$ are assumed as normal distributions. These measurement error distributions were calibrated in a previous study using the same data set, assuming Gaussian distributions with zero means and variances $\sigma_{D,p}^2$ and $\sigma_{D,Q}^2$, respectively [39]. Equations (5) and (6), rewritten for Piston theory and Eckert's reference temperature, are given in Eq. (26):

$$p_D = p_4 + \varepsilon_{D,p} = p_4^{\mathrm{PT}} + \delta_p^{\mathrm{PT}} + \varepsilon_{D,p} \tag{26}$$

$$Q_D = Q_4 + \varepsilon_{D,Q} = Q_4^{\mathrm{ERT}} + \delta_Q^{\mathrm{ERT}} + \varepsilon_{D,Q} \tag{27}$$

Figure 16 shows the Bayesian network corresponding to the relationships between the aerodynamic pressure and heat flux model predictions along the panel (p_4, Q_4), aerothermal data (p_D, Q_D), model inputs (p_1, M_1), random model inputs (T_1, T_w), measurement errors ($\varepsilon_{D,p}$, $\varepsilon_{D,Q}$), and discrepancy terms for calibration (δ_p^{PT}, δ_Q^{ERT}).

The discrepancy models are chosen as a function of dome slope, which follows previous work by the authors [39] and given in Eqs. (28) and (29). The prior uniform distribution parameters for the uncertain model discrepancy coefficients are given in Table 3:

$$\delta_p^{\mathrm{PT}} = b_0^{\mathrm{PT}} + b_1^{\mathrm{PT}} \frac{\partial w}{\partial x} + b_2^{\mathrm{PT}} \left(\frac{\partial w}{\partial x} \right)^2 \tag{28}$$

$$\delta_Q^{\mathrm{ERT}} = c_0^{\mathrm{ERT}} + c_1^{\mathrm{ERT}} \frac{\partial w}{\partial x} + c_2^{\mathrm{ERT}} \left(\frac{\partial w}{\partial x} \right)^2 \tag{29}$$

A global sensitivity analysis using these prior model discrepancy coefficients was performed in [39] and showed that the sensitivity of Q_4 to δ_p^{PT} and δ_Q^{ERT} is 0.592 and 0.333, respectively. These sensitivities correspond to a dependence coefficient of 1.3 in reference to Fig. 4, indicating that a segmented calibration strategy could be viable without significantly compromising calibration accuracy. (This is, of course, very rough preliminary reasoning because the analytical example is not the same as the current problem.) In a segmented calibration procedure, the aerothermal calibration parameters are subdivided into pressure and heat flux calibration sets $\mathbf{\Phi}_p = [b_0^{\mathrm{PT}}, b_1^{\mathrm{PT}}, b_2^{\mathrm{PT}}]$ and $\mathbf{\Phi}_Q = [c_0^{\mathrm{ERT}}, c_1^{\mathrm{ERT}}, c_2^{\mathrm{ERT}}]$. The next subsection will describe the high-speed wind-tunnel tests and aerothermal data that will be used for model calibration.

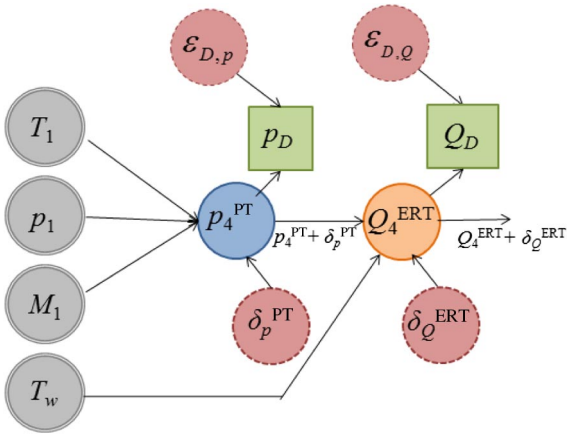

Fig. 16 Bayesian network for aerothermal models and experiments.

Table 3 Prior distributions for uncertain parameters

Parameter	Lower bound	Upper bound
b_0^{PT} Pa	−4e2	4e2
b_1^{PT} Pa	−1e4	1e4
b_2^{PT} Pa	−1e5	1e5
c_0^{ERT} W/m^2	−2e4	2e4
c_1^{ERT} W/m^2	−5e5	5e5
c_2^{ERT} W/m^2	−5e6	5e6

Table 4 Experimental conditions for three tests by Glass and Hunt [37] with different H/D ratios

Test	p_1, Pa	M_1	H/D
Run 30	654.9	6.60	0.028
Run 31	648.0	6.60	0.013
Run 32	645.9	6.60	0.006

B. Aerothermal Wind-Tunnel Data

Tests conducted by Glass and Hunt in 1986 at NASA's 8 ft high-temperature wind tunnel investigated the thermal and structural loads on body panels in hypersonic environments [37]. These tests measured the aerodynamic pressure and heating on spherical dome protuberances that simulated deformed aircraft panels. The flow conditions for the tests of interest had a turbulent boundary layer at the panel location and the panel holder had a sharp leading edge, similar to the representative hypersonic vehicle depicted in Fig. 11. The spherical domes were constructed at three different height-to-diameter H/D ratios with a dome diameter of 14 in. (0.356 m). The freestream hypersonic flow conditions and dimensions of the three spherical dome configurations considered in this analysis are presented in Table 4.

Along with the Mach number M_1 and freestream pressure p_1 for each run, the data report both the aerodynamic pressure p_D and aerodynamic heat flux Q_D at 58 instrumented locations on the spherical dome. For the purposes of this analysis, only 11 points along the dome centerline are considered. Therefore, there are $N_p = N_Q = 33$ data points total (i.e., 11 points on three domes) of aerodynamic pressure and heat flux.

Note, however, that the freestream temperature T_1 (a shared model input, explained in Sec. II) and the initial wall temperature T_w were left unreported in the Glass and Hunt data [37]. The lack of information on these two parameters presents epistemic input uncertainty; however, sensitivity analyses from related studies by DeCarlo et al. [39] and Smarslok et al. [40] have determined that a 10% coefficient of variation in these parameters was not a significant source of uncertainty in pressure or heat flux. As such, they will not be considered for calibration; thus, only the model discrepancy parameters identified in Sec. IV.A are considered for calibration.

The data are subdivided into calibration and validation sets. In this paper, calibrations are performed using data from two domes with lower H/D ratios (i.e., runs 31 and 32) and then the predictions based on the results of the two calibration strategies are compared against the pressure and heat flux measurements from run 30, which had the highest H/D ratio. Further, a feature of run 31 is exploited to test the

Table 5 Calibration cases with varying data available on p_D and Q_D

Case	N_p	N_Q
1	3	3
2	3	22
3	22	3
4	22	22

effects of data availability on calibration. The front, back, and middle points of the run 31 test set represent the most positive, most negative, and zero slopes. These three points are used to illustrate the sparse data case; in contrast, the abundant data case has 22 data values (i.e., at 11 locations on each dome). The four calibration cases considered are shown in Table 5.

C. Simultaneous and Segmented Calibration Results

Simultaneous and segmented calibrations for error parameters δ_p^{PT} and δ_p^{ERT} were conducted. For simultaneous calibration, 50,000 samples of the posterior distributions were generated using slice sampling [18]. Similarly, for segmented calibration, 50,000 samples were generated for each segment.

As a representative parameter for comparing the results of the segmented and simultaneous calibration, the posterior distributions of the piston theory error parameter b_0^{PT} with $N_p = 3$ and 22 is shown in Fig. 17. As was the case in the analytical example in Sec. III, the posterior distributions from the first calibration are not affected by the calibration type or the model dependence but by the amount of data available. Similar to the analytical example with low dependence coefficient c, the amount of downstream data N_Q does not impact the posterior PDFs of b_0^{PT}.

In a segmented strategy, the posterior distributions of b_0^{PT}, b_1^{PT}, and b_2^{PT} propagate forward in the next calibration and do not change; the effect of this is seen in the downstream calibration of c_0^{ERT} shown in Fig. 18. For the aerothermal example, when there is limited data for the first calibration but abundant data for the second calibration ($N_p = 3$, $N_Q = 22$), the segmented calibration strategy does not capture c_0^{ERT} as precisely as the simultaneous strategy. This parallels the conclusions of the analytical example when considering low model dependence (Fig. 9).

The posterior distributions of $\mathbf{\Phi}_p$ and $\mathbf{\Phi}_Q$ are propagated through piston theory and Eckert's reference temperature models and compared against pressure and heat flux data from run 30 in Figs. 19 and 20, respectively. In both figures, the prediction variance is smaller at the dome center and increases toward the edges, due to Eqs. (26) and (27). The slope is zero at the dome center, and thus only the first terms in Eqs. (26) and (27) contribute to the prediction variance; as we move toward the edges, the slopes are nonzero and increasing, thus increasing the prediction variance.

Similar to the posterior results for b_0^{PT} in Fig. 17, the posterior pressure prediction is affected by the amount of data N_p; the prediction bounds are wider for the sparse data case. The prediction bounds from both calibration strategies are generally similar. The slight differences toward the edges are explained by the differences in the mean predictions and the correlation coefficients among the calibration parameters estimated by the two strategies.

However, uncertainty in the downstream heat flux prediction increases from the segmented calibration. For example, when $N_p = 3$ in Fig. 20, the variance at the dome edges from segmented calibration is significantly greater than those from the simultaneous calibration. When there is ample N_p data, however, the segmented and simultaneous strategies have small differences. These differences are quantified in Sec. IV.D using the Bayes factor.

The explanation for the differences between Eckert's reference temperature predictions in Fig. 20 is that segmented calibration ignores negative correlation between $\mathbf{\Phi}_p$ and $\mathbf{\Phi}_Q$, as discussed in Sec. III. These correlations are significant in the simultaneous posterior samples and are dependent on the relative amount of observed data. For the data cases considered, the correlation coefficients between parameters b_0^{PT} and c_0^{ERT} are listed in Table 6. Not accounting for these correlations in a segmented strategy leads to additional variance in downstream predictions, similar to the analytical example in Sec. III.

D. Comparison of Calibration Strategies

To assess the effectiveness of the segmented calibration methodology compared with the simultaneous procedure, this subsection compares the accuracy and computational effort of the segmented and simultaneous calibration methods. Accuracy is compared using Bayes factors, and computational effort is compared using convergence of the K-L divergence metric.

Values of Bayes factors B are computed using Eq. (14) and are obtained at each run 30 dome location. Table 7 shows average B values over all locations, B value at the dome center, and B value at the front edge of the dome. In the last column, the Bayes factors for the pressure and heat flux prediction (B_p and B_Q) at each location are multiplied and averaged over all locations to compute $B_{\mathrm{total,ave}}$. A Bayes factor greater than one indicates that the data favor the segmented calibration method.

Most of the Bayes factors are close to one, implying that a segmented calibration strategy results in no significant loss of

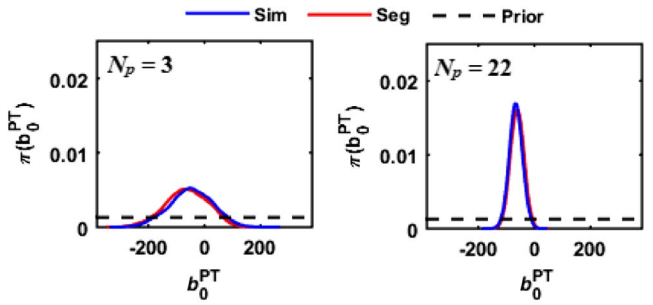

Fig. 17 Prior and posterior distributions for b_0^{PT} from segmented and simultaneous calibration.

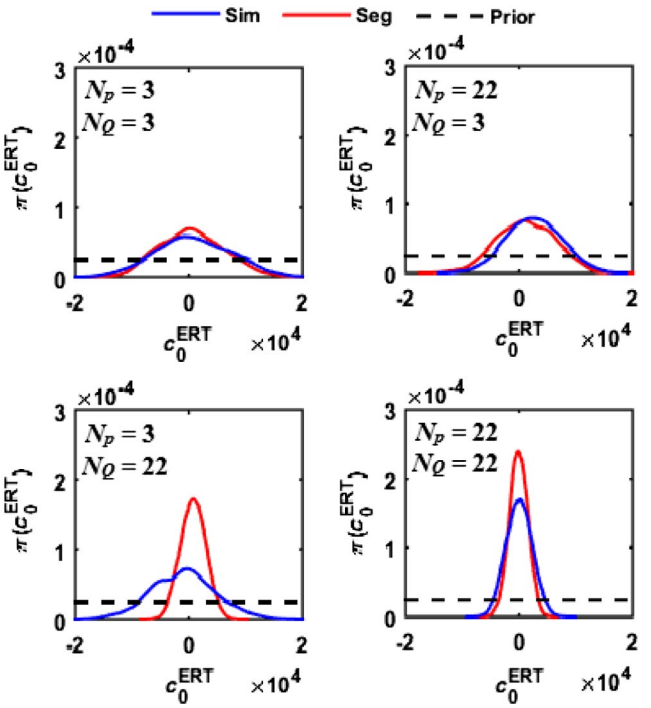

Fig. 18 Prior and posterior distributions for c_0^{ERT} from segmented and simultaneous calibration.

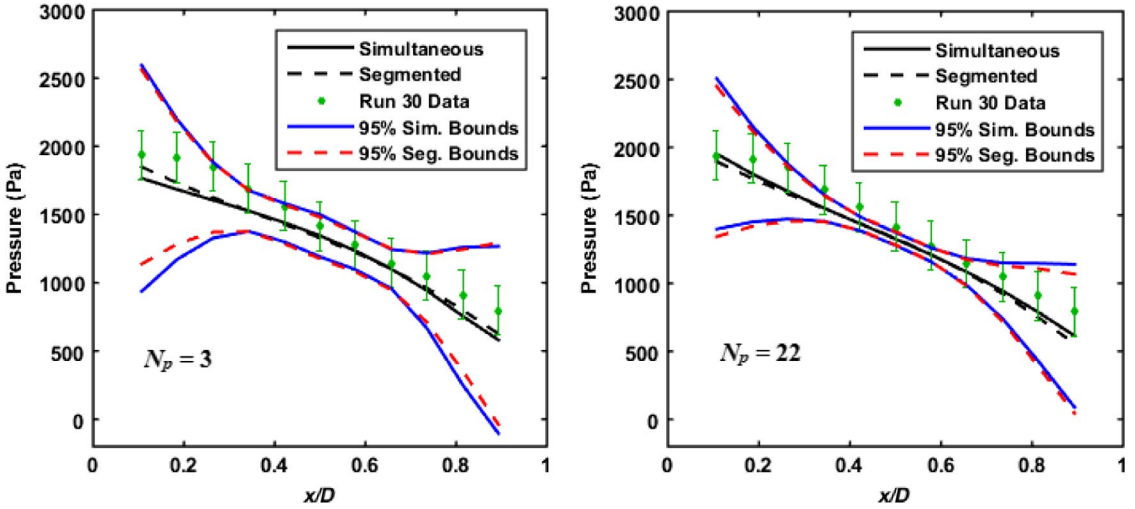

Fig. 19 Pressure prediction vs observation across dome when $N_p = 3$ and 22.

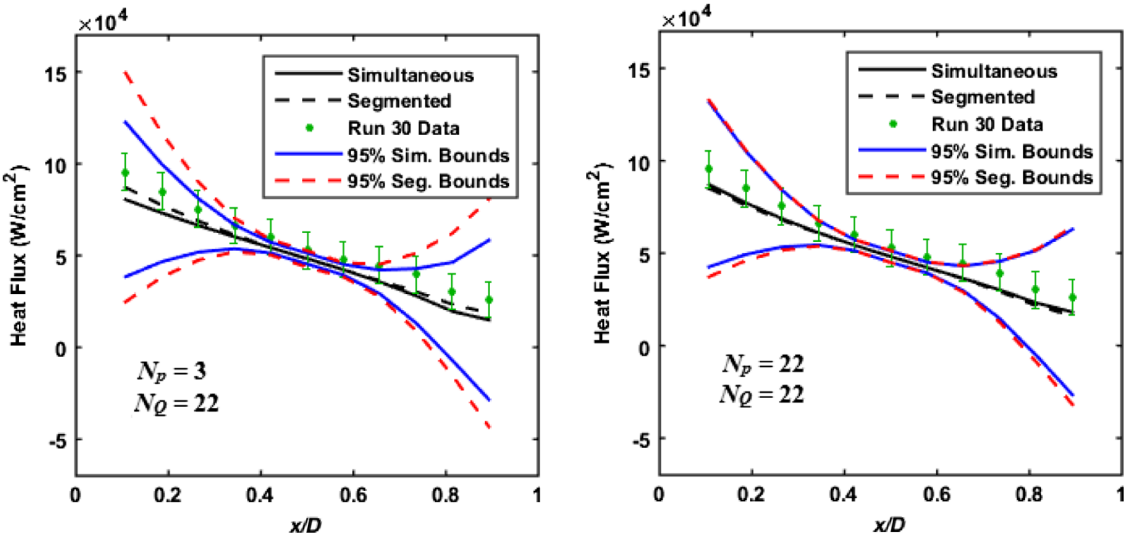

Fig. 20 Eckert's reference temperature predictions across dome from posterior distributions when $N_p = 22$.

accuracy for this problem. Substantial difference between competing models is only indicated by Bayes factors greater than three, as pointed out by Jeffreys [22].

Table 6 Correlation coefficients between b_0^{PT} and c_0^{ERT} from simultaneous calibration

N_p	N_Q	ρ
3	3	−0.74
3	22	−0.97
33	3	−0.28
33	22	−0.74

Table 7 Bayes factors across the dome for pressure and heat flux predictions

N_p	N_Q	$B_{p,\mathrm{ave}}$	$B_{p,\mathrm{mid}}$	$B_{p,\mathrm{front}}$	$B_{Q,\mathrm{ave}}$	$B_{Q,\mathrm{mid}}$	$B_{Q,\mathrm{front}}$	$B_{\mathrm{combined,ave}}$
3	3	1.06	0.92	1.22	1.04	0.83	1.02	1.11
3	22	1.07	0.85	1.17	1.02	0.95	0.84	1.08
22	3	0.94	1.04	0.99	0.99	0.90	0.96	0.93
22	22	0.95	1.02	0.97	0.94	1.01	0.91	0.90

Calibration convergence rates are computed using K-L divergence, presented in Eq. (15), with the integral being evaluated numerically using Monte Carlo integration with the slice samples generated from calibration, as explained in Sec. III.D. For the aerothermal calibration, convergence was tested after every 1000 slice samples and assumed to be reached when $\log(D_{\mathrm{KL},i}) \leq -8$. It is seen that the convergence rate is not affected by the amount of observed data. The average number of samples (considering four different data availability cases) at which the simultaneous and segmented procedures reached convergence are presented in Table 8.

Table 8 shows that, to obtain convergence in simultaneous calibration, both models must be evaluated 39,000 times. Whereas for segmented calibration to obtain convergence, only 10,000 evaluations of each model were required, thus indicating substantial savings in computational effort.

Table 8 Average number of samples to convergence

Procedure	Model	Samples
Simultaneous	Both models	39,000
Segmented	Piston theory	10,000
	Eckert's reference temperature	10,000

V. Conclusions

A segmented Bayesian model calibration approach for multidisciplinary models was investigated for models in different disciplines as an alternative to full simultaneous calibration to reduce the computational cost. The study included identifying the required characteristics of calibration (i.e., low model dependence and ample data specifically on the first model output), identifying the appropriate uncertain parameters and errors for calibration with the segmented process and assessing the efficiency and accuracy of segmented model calibration.

The aerothermal problem was segmented into piston theory and Eckert's reference temperature model components. To quantify the viability and potential benefit of isolating calibrations of models in the Bayesian network, segmented and simultaneous calibration were compared using the Kullback–Leibler (K-L) divergence and Bayes factor metrics. The K-L divergence was used to monitor calibration convergence, and the Bayes factor was used to assess the accuracy.

The following insights were obtained based on comparison between the two calibration approaches, using the analytical example and the aerothermal application problem:

1) As the coupling strength between the two models increases, the segmented approach loses accuracy for both upstream and downstream predictions.

2) When there is limited data available on the first model output, more uncertainty propagates downstream from the calibration of the first model parameters affecting downstream prediction confidence. Furthermore, a simultaneous strategy has the opportunity to use downstream data to reduce the uncertainty in upstream parameters. This effect becomes apparent in limited data cases as dependence between models increases.

3) Parameter correlations inherent in the simultaneous calibration are ignored in the segmented approach, which yields greater downstream prediction uncertainty.

4) For problems where coupling strength is not readily obvious (e.g., the aerothermal example), a global sensitivity analysis can indicate the coupling strength.

5) When the two models have shared parameters, the shared parameters are calibrated twice in a segmented calibration strategy (i.e., the posterior from the first calibration is the prior for the second calibration). This offers a second opportunity for uncertainty reduction in the shared parameter.

6) The calibration convergence comparison using K-L divergence indicates higher computational efficiency of the segmented approach. For the application problem, the reduction in the number of evaluations of each model using the segmented approach compared with simultaneous calibration was 74.4%. Further, in terms of accuracy comparison, both strategies yielded similar posterior predictions, as indicated by the Bayes factors.

Further investigation into the tradeoffs between accuracy and efficiency between the segmented and simultaneous calibration methods is needed, especially when different models require different computational effort. Additional work on multidisciplinary model calibration needs to address transient simulations and feedback coupling between disciplinary models. In the presence of feedback coupling, sensitivity analyses and forward propagation of uncertainty are not straightforward, unlike the examples presented in this work. Future work may also address resource allocation for data collection in the context of multidisciplinary model calibration and its connection to the preferred calibration strategy.

Appendix A: Analytical Posterior Distributions

Analytical expressions for the posterior distributions for segmented and simultaneous calibration of θ_1 and θ_2 are derived next using the assumption of conjugate distributions [25]. Both the prior and posterior of the calibration are assumed to be normal here, only for the analytical example in Sec. III.

A.1. Segmented Calibration

The segmented Bayesian calibration of θ_1 is shown in Eq. (A1). The likelihood in Eq. (A1) can be derived to be as Eq. (A2), assuming normal observation error with zero mean and known variance σ_{D1}^2 [41]. Note that the prediction from the first model is $y_1(\theta_1) = \theta_1$, as in Sec. III:

$$\pi(\theta_1|y_{D1}) \propto L(\theta_1)\pi(\theta_1) \tag{A1}$$

$$L(\theta_1) \propto \prod_{i=1}^{N_1} \pi(y_{D1,i}|\theta_1) \propto \exp\left[-\frac{1}{2}\frac{(\theta_1 - \overline{y_{D1}})^2}{\sigma_{D1}^2/N_1}\right] \tag{A2}$$

Multiplying Eq. (A2) by the normal prior of θ_1, the normal posterior mean $\mu_{\theta 1|D1}$ and variance $\sigma_{\theta 1|D1}^2$ are derived as Eqs. (A3) and (A4) using the assumption of conjugate prior and posterior distributions:

$$\mu_{\theta 1|D1} = \frac{N_1\sigma_{\theta 1}^2\overline{y_{D1}} + \mu_{\theta 1}\sigma_{D1}^2}{N_1\sigma_{\theta 1}^2 + \sigma_{D1}^2} \tag{A3}$$

$$\sigma_{\theta 1|D1}^2 = \frac{\sigma_{\theta 1}^2\sigma_{D1}^2}{N_1\sigma_{\theta 1}^2 + \sigma_{D1}^2} \tag{A4}$$

The Bayesian formulation and likelihood for the calibration of θ_2 are shown in Eqs. (A5) and (A6). The prediction from the second model is $y_2(\theta_1, \theta_1) = c\theta_1 + \theta_2$. In segmented calibration, θ_1 has been calibrated earlier and is now treated as aleatory and not updated. Thus, the likelihood $L(\theta_2)$ in Eq. (A6) includes the posterior distribution of $\theta_{1|D1}$:

$$\pi(\theta_2|y_{D2}) \propto L(\theta_2)\pi(\theta_2) \tag{A5}$$

$$\begin{aligned} L(\theta_2) &\propto \prod_{i=1}^{N_2} \pi(y_{D2,i}|c\theta_{1|D1} + \theta_2) \\ &\propto \exp\left[-\frac{1}{2}\frac{(c\mu_{\theta 1|D1} + \theta_2 - \overline{y_{D2}})^2}{(c^2\sigma_{\theta 1|D1} + \sigma_{D2}^2)/N_2}\right] \end{aligned} \tag{A6}$$

Multiplying Eq. (A6) by the normal prior of θ_2, the posterior mean $\mu_{\theta 2|D2}$ and variance $\sigma_{\theta 2|D2}^2$ are derived as Eqs. (A7) and (A8), respectively, similar to the derivations of Eqs. (A3) and (A4):

$$\mu_{\theta 2|D2} = \frac{N_2\sigma_{\theta 2}^2(\overline{y_{D2}} - c\mu_{\theta 1|D1}) + \mu_{\theta 2}(c^2\sigma_{\theta 1|D1}^2 + \sigma_{D2}^2)}{N_2\sigma_{\theta 2}^2 + (c^2\sigma_{\theta 1|D1}^2 + \sigma_{D2}^2)} \tag{A7}$$

$$\sigma_{\theta 2|D2}^2 = \frac{\sigma_{\theta 2}^2(c^2\sigma_{\theta 1|D1}^2 + \sigma_{D2}^2)}{N_2\sigma_{\theta 2}^2 + (c^2\sigma_{\theta 1|D1}^2 + \sigma_{D2}^2)} \tag{A8}$$

The posterior statistics in Eqs. (A7) and (A8) are derived by ignoring the correlation between θ_1 and θ_2, which is the essential feature of segmented calibration. Next, the posterior statistics of θ_1 and θ_2 are propagated to the prediction of y_2 as in Eq. (A9) and (A10):

$$\mu_{y2}^{\text{seg}} = c\mu_{\theta 1D1} + \mu_{\theta 2|D2} \tag{A9}$$

$$\sigma_{y2}^{2,\text{seg}} = c^2\sigma_{\theta1|D1}^2 + \sigma_{\theta2|D1}^2 \tag{A10}$$

A.2. Simultaneous Calibration

The simultaneous formulation of Bayesian calibration is shown in Eq. (A11) and the joint likelihood is shown in Eq. (A12):

$$\pi(\theta_1, \theta_2|y_{D1}, y_{D2}) \propto L(\theta_1, \theta_2)\pi(\theta_1, \theta_2) \tag{A11}$$

$$\begin{aligned} L(\theta_1, \theta_2) &\propto \pi(y_{D1}, y_{D2}|\theta_1, \theta_2) \\ &\propto \pi(y_{D1}|\theta_1)\pi(y_{D2}|c\theta_1 + \theta_2) \\ &\propto \exp\left[-\frac{1}{2}\frac{(\theta_1 - \overline{y_{D1}})^2}{\sigma_{D1}^2/N_1}\right] \exp\left[-\frac{1}{2}\frac{N_2(c\theta_1 + \theta_2 - \overline{y_{D2}})^2}{\sigma_{D2}^2/N_2}\right] \end{aligned} \tag{A12}$$

Using the result in Eq. (A2), the likelihood in Eq. (A12) is multiplied by the normal prior of θ_1 and θ_2. The joint posterior means and variances of θ_1 and θ_2 and correlation coefficient between θ_1 and θ_2 can be derived as follows:

$$\mu_{\theta1|D1,D2} = \frac{N_2 c\sigma_{\theta1}^2\sigma_{D1}^2(\overline{y_{D2}} - \mu_{\theta2}) + (N_2\sigma_{\theta2}^2 + \sigma_{D2}^2)(N_1\overline{y_{D1}}\sigma_{\theta1}^2 + \mu_{\theta1}\sigma_{D1}^2)}{N_2c^2\sigma_{\theta1}^2\sigma_{D1}^2 + (N_2\sigma_{\theta2}^2 + \sigma_{D2}^2)(N_1\sigma_{\theta1}^2 + \sigma_{D1}^2)} \tag{A13}$$

$$\sigma_{\theta1|D1,D2}^2 = \frac{\sigma_{\theta1}^2\sigma_{D1}^2(N_2\sigma_{\theta2}^2 + \sigma_{D2}^2)}{N_2c^2\sigma_{\theta1}^2\sigma_{D1}^2 + (N_2\sigma_{\theta2}^2 + \sigma_{D2}^2)(N_1\sigma_{\theta1}^2 + \sigma_{D1}^2)} \tag{A14}$$

$$\mu_{\theta2|D1,D2} = \frac{N_2\sigma_{\theta2}^2N_1\sigma_{\theta1}^2(\overline{y_{D2}} - c\overline{y_{D1}}) + N_2\sigma_{\theta2}^2\sigma_{D1}^2(\overline{y_{D2}} - c\mu_{\theta1}) + \mu_{\theta2}(N_2c^2\sigma_{\theta1}^2\sigma_{D1}^2 + \sigma_{D2}^2(N_1\sigma_{\theta1}^2 + \sigma_{D1}^2))}{N_2c^2\sigma_{\theta1}^2\sigma_{D1}^2 + (N_1\sigma_{\theta1}^2 + \sigma_{D1}^2)(N_2\sigma_{\theta2}^2 + \sigma_{D2}^2)} \tag{A15}$$

$$\sigma_{\theta2|D1,D2}^2 = \frac{\sigma_{\theta2}^2N_2c^2\sigma_{\theta1}^2\sigma_{D1}^2 + \sigma_{D2}^2\sigma_{\theta2}^2(N_1\sigma_{\theta1}^2 + \sigma_{D1}^2)}{N_2c^2\sigma_{\theta1}^2\sigma_{D1}^2 + (N_1\sigma_{\theta1}^2 + \sigma_{D1}^2)(N_2\sigma_{\theta2}^2 + \sigma_{D2}^2)} \tag{A16}$$

$$\rho(\theta_{1|D1,D2}, \theta_{2|D1,D2}) = \frac{-N_2c\sigma_{\theta2}\sigma_{\theta1}\sigma_{D1}}{\sqrt{(N_2c^2\sigma_{\theta1}^2\sigma_{D1}^2 + \sigma_{\theta2}^2(N_1\sigma_{\theta1}^2 + \sigma_{D1}^2))(N_2\sigma_{\theta2}^2 + \sigma_{D2}^2)}} \tag{A17}$$

Next, the posterior statistics of θ_1 and θ_2 are propagated to the prediction of y_2 to obtain

$$\mu_{y2}^{\text{sim}} = c\mu_{\theta1D1,D2} + \mu_{\theta2|D2,D2} \tag{A18}$$

$$\begin{aligned} \sigma_{y2}^{2,\text{sim}} &= c^2\sigma_{\theta1|D1,D2}^2 + \sigma_{\theta2|D1,D2}^2 \\ &\quad + 2c\rho(\theta_{1|D1,D2}, \theta_{2|D1,D2})\sigma_{\theta1|D1,D2}\sigma_{\theta2|D1,D2} \end{aligned} \tag{A19}$$

A.3. Segmented Calibration with Shared Parameters θ_1

In this case, θ_1 is a shared parameter for which the posterior from the first calibration is the prior for the second calibration. The Bayesian formulation and the likelihood are shown in Eqs. (A20) and (A21):

$$\pi(\theta_1, \theta_2|y_{D1}, y_{D2}) \propto L(\theta_1, \theta_2)\pi(\theta_2)\pi(\theta_1|y_{D1}) \tag{A20}$$

$$L(\theta_1, \theta_2) \propto \exp\left[-\frac{1}{2}\frac{N_2(\overline{y_{D2}} - c\theta_1 - \theta_2)^2}{\sigma_{D2}^2}\right] \tag{A21}$$

Multiplying Eq. (A21) by the normal prior of θ_2 and $\pi(\theta_1|y_{D1})$, the joint posterior means and variances of θ_1 and θ_2 and correlation coefficient between θ_1 and θ_2 are derived as follows:

$$\mu_{\theta1|D1,D2} = \frac{N_2c(\overline{y_{D2}} - c\mu_{\theta2})\sigma_{\theta1|D1}^2 + \mu_{\theta1|D1}(N_2\sigma_{\theta2}^2 + \sigma_{D2}^2)}{N_2(c^2\sigma_{\theta1|D1}^2 + \sigma_{\theta2}^2) + \sigma_{D2}^2} \tag{A22}$$

$$\sigma_{\theta1|D1,D2}^2 = \frac{\sigma_{\theta1|D1}^2(N_2\sigma_{\theta2}^2 + \sigma_{D2}^2)}{N_2(c^2\sigma_{\theta1|D1}^2 + \sigma_{\theta2}^2) + \sigma_{D2}^2} \tag{A23}$$

$$\mu_{\theta2|D1,D2} = \frac{N_2(\overline{y_{D2}} - c\mu_{\theta1|D1})\sigma_{\theta2}^2 + \mu_{\theta2}(N_2c^2\sigma_{\theta1|D1}^2 + \sigma_{D2}^2)}{N_2(c^2\sigma_{\theta1|D1}^2 + \sigma_{\theta2}^2) + \sigma_{D2}^2} \tag{A24}$$

$$\sigma_{\theta2|D1,D2}^2 = \frac{\sigma_{\theta2}^2(N_2c^2\sigma_{\theta1|D1}^2 + \sigma_{D2}^2)}{N_2(c^2\sigma_{\theta1|D1}^2 + \sigma_{\theta2}^2) + \sigma_{D2}^2} \tag{A25}$$

$$\rho(\theta_1, \theta_2)_{\text{sim}} = \frac{-N_2c\sigma_{\theta2}\sigma_{\theta1|D1}}{\sqrt{(N_2c^2\sigma_{\theta1|D1}^2 + \sigma_{\theta2}^2)(N_2\sigma_{\theta2}^2 + \sigma_{D2}^2)}} \tag{A26}$$

Acknowledgments

This research was partly funded by the National Defense Science and Engineering Graduate fellowship and the U.S. Air Force Office of Scientific Research (AFOSR). The authors gratefully acknowledge the support of AFOSR program managers Fariba Fahroo and David Stargel. The authors also acknowledge valuable technical discussions with You Ling and Joshua Mullins during their time as Vanderbilt graduate students.

References

[1] Sankararaman, S., "Uncertainty Quantification and Integration," Ph.D. Dissertation, Vanderbilt Univ., Nashville, TN, 2012.

[2] Hastie, T., Tibshirani, R., and Friedman, J., *The Elements of Statistical Learning*, 2nd ed., Springer–Verlag, New York, 2009, pp. 337–387.

[3] Mahadevan, S., Zhang, R., and Smith, N., "Bayesian Networks for System Reliability Reassessment," *Structural Safety*, Vol. 23, No. 3, 2001, pp. 231–251. doi:10.1016/S0167-4730(01)00017-0

[4] Wang, S., Chen, W., and Tsui, K., "Bayesian Validation of Computer Models," *Technometrics*, Vol. 51, No. 4, 2009, pp. 439–451.

[5] Sarkar, S., Kosson, D. S., Mahadevan, S., Meeussen, J. C. L., Van Der Sloot, H., Arnold, J. R., and Brown, K. G., "Bayesian Calibration of Thermodynamic Parameters for Geochemical Speciation Modeling of

Cementitious Materials," *Cement and Concrete Research*, Vol. 42, No. 7, 2012, pp. 889–902. doi:10.1016/j.cemconres.2012.02.004

[6] Li, C., and Mahadevan, S., "Role of Calibration, Validation, and Relevance in Multi-Level Uncertainty Integration," *Reliability Engineering & System Safety*, Vol. 148, April 2016, pp. 32–43. doi:10.1016/j.ress.2015.11.013

[7] Urbina, A., Mahadevan, S., and Paez, T. L., "Quantification of Margins and Uncertainties of Complex Systems in the Presence of Aleatoric and Epistemic Uncertainty," *Reliability Engineering & System Safety*, Vol. 96, No. 9, 2011, pp. 1114–1125. doi:10.1016/j.ress.2010.08.010

[8] Sankararaman, S., and Mahadevan, S., "Integration of Model Verification, Validation, and Calibration for Uncertainty Quantification in Engineering Systems," *Reliability Engineering & System Safety*, Vol. 138, June 2015, pp. 194–209. doi:10.1016/j.ress.2015.01.023

[9] Roy, C. J., and Oberkampf, W. L., "A Comprehensive Framework for Verification, Validation, and Uncertainty Quantification in Scientific Computing," *Computer Methods in Applied Mechanics and Engineering*, Vol. 200, Nos. 25–28, 2011, pp. 2131–2144.

[10] Sankararaman, S., Ling, Y., and Mahadevan, S., "Uncertainty Quantification and Model Validation of Fatigue Crack Growth Prediction," *Engineering Fracture Mechanics*, Vol. 78, No. 7, 2011, pp. 1487–1504. doi:10.1016/j.engfracmech.2011.02.017

[11] Sankararaman, S., and Mahadevan, S., "Likelihood-Based Approach to Multidisciplinary Analysis Under Uncertainty," *Journal of Mechanical Design*, Vol. 134, No. 3, 2012, Paper 031008. doi:10.1115/1.4005619

[12] Bliznyuk, N., Ruppert, D., Shoemaker, C., Regis, R., Wild, S., and Mugunthan, P., "Bayesian Calibration and Uncertainty Analysis for Computationally Expensive Models Using Optimization and Radial Basis Function Approximation," *Journal of Computational and Graphical Statistics*, Vol. 17, No. 2, 2008, pp. 270–294.

[13] Ling, Y., and Mahadevan, S., "Challenging Issues in Bayesian Calibration of Multi-Physics Models," *54th AIAA/ASME/ASCE/AHS/ASC Structures, Structural Dynamics, and Materials Conference*, AIAA Paper 2013-1874, 2013.

[14] Kullback, S., and Leibler, R. A., "On Information and Sufficiency," *Annals of Mathematical Statistics*, Vol. 22, No. 1, 1951, pp. 79–86. doi:10.1214/aoms/1177729694

[15] Novak, E., and Woźniakowski, H., "Approximation of Infinitely Differentiable Multivariate Functions is Intractable," *Journal of Complexity*, Vol. 25, No. 4, 2009, pp. 398–404. doi:10.1016/j.jco.2008.11.002

[16] Hastings, W. K., "Monte Carlo Sampling Methods Using Markov Chains and Their Applications," *Biometrika*, Vol. 57, No. 1, 1970, pp. 97–109. doi:10.1093/biomet/57.1.97

[17] Casella, G., and George, E. I., "Explaining the Gibbs Sampler," *American Statistician*, Vol. 46, No. 3, Aug. 1992, pp. 167–174.

[18] Neal, R. M., "Slice Sampling," *Annals of Statistics*, Vol. 31, No. 3, 2003, pp. 705–767. doi:10.1214/aos/1056562461

[19] Mahadevan, S., and Liang, B., "Error and Uncertainty Quantification and Sensitivity Analysis in Mechanics Computational Models," *International Journal for Uncertainty Quantification*, Vol. 1, No. 2, 2011, pp. 147–161. doi:10.1615/IntJUncertaintyQuantification.v1.i2

[20] Saltelli, A., *Global Sensitivity Analysis: The Primer*, Vol. 76, No. 3, John Wiley & Sons, Inc., Hoboken, NJ, 2008, pp. 1–452.

[21] Sobol, I. M., "Global Sensitivity Indices for Nonlinear Mathematical Models and Their Monte Carlo Estimates," *Mathematics and Computers in Simulation*, Vol. 55, Nos. 1–3, 2001, pp. 271–280. doi:10.1016/S0378-4754(00)00270-6

[22] Jeffreys, H., *Theory of Probability*, 3rd ed., Oxford Univ. Press, New York, NY, 1961, pp. 1–470.

[23] O'Hagan, A., "Fractional Bayes Factors for Model Comparison," *Journal of the Royal Statistical Society, Series B*, Vol. 57, No. 1, 1995, pp. 99–138.

[24] Ling, Y., and Mahadevan, S., "Quantitative Model Validation Techniques: New Insights," *Reliability Engineering & System Safety*, Vol. 111, March 2013, pp. 217–231. doi:10.1016/j.ress.2012.11.011

[25] Ang, A. H. S., and Tang, W. H., *Probability Concepts in Engineering Planning and Design*, Vol. 1, Wiley, New York, 1975, pp. 1–424.

[26] Ostoich, C., "Aerothermal and Aeroelastic Response Prediction of Aerospace Structures in High-Speed Flows Using Direct Numerical Simulation," Ph.D. Dissertation, Univ. of Illinois, Urbana-Champaign, 2013.

[27] Crowell, A. R., Mcnamara, J. J., and Miller, B. A., "Surrogate Based Reduced-Order Aerothermodynamic Modeling for Structural Response Prediction at High Mach Numbers," *52nd AIAA/ASME/ASCE/AHS/ASC Structures, Structural Dynamics and Materials Conference*, AIAA Paper 2011-2014, April 2011.

[28] McNamara, J. J., Friedmann, P. P., Powell, K. G., Thuruthimattam, B. J., and Bartels, R. E., "Aeroelastic and Aerothermoelastic Behavior in Hypersonic Flow," *AIAA Journal*, Vol. 46, No. 10, Oct. 2008, pp. 2591–2610. doi:10.2514/1.36711

[29] Thornton, E. A., and Dechaumphai, P., "Coupled Flow, Thermal, and Structural Analysis of Aerodynamically Heated Panels," *Journal of Aircraft*, Vol. 25, No. 11, Nov. 1988, pp. 1052–1059. doi:10.2514/3.45702

[30] Kontinos, D., "Coupled Thermal Analysis Method with Application to Metallic Thermal Protection Panels," *Journal of Thermophysics and Heat Transfer*, Vol. 11, No. 2, April 1997, pp. 173–181. doi:10.2514/2.6249

[31] Blevins, R. D., Bofilios, D., Holehouse, I., Hwa, V. W., Tratt, M. D., Laganelli, A. L., Pozefsky, P., and Pierucci, M., "Thermo-Vibro-Acoustic Loads and Fatigue of Hypersonic Flight Vehicle Structure—Phase II Report," Rohr Industries, Inc., RHR-89-202, Nov. 1989.

[32] Blevins, R. D., Holehouse, I., and Wentz, K. R., "Thermoacoustic Loads and Fatigue of Hypersonic Vehicle Skin Panels," *Journal of Aircraft*, Vol. 30, No. 6, Nov. 1993, pp. 971–978. doi:10.2514/3.46441

[33] Farokhi, S., *Aircraft Propulsion*, 2nd ed., Wiley, Hoboken, NJ, 2014, pp. 1–1048.

[34] Falkiewicz, N., and Cesnik, C. E. S., "Enhanced Modal Solutions for Structural Dynamics in Aerothermoelastic Analysis," AIAA Paper 2011-1963, April 2011.

[35] Ashley, G., and Zartarian, H., "Piston Theory: A New Aerodynamic Tool for the Aeroelastician," *Journal of the Aeronautical Sciences*, Vol. 23, No. 12, 1956, pp. 1109–1118. doi:10.2514/8.3740

[36] Eckert, E. R. G., "Engineering Relations for Heat Transfer and Friction in High-Velocity Laminar and Turbulent Boundary-Layer Flow over Surfaces with Constant Pressure and Temperature," *Transactions of the American Society of Mechanical Engineers*, Vol. 78, No. 6, 1956, pp. 1273–1283.

[37] Glass, C. E., and Hunt, L. R., "Aerothermal Tests of Spherical Dome Protuberances on a Flat Plate at a Mach Number of 6.5," NASA TP-2631, 1986.

[38] Culler, A. J., and Mcnamara, J. J., "Fluid-Thermal-Structural Modeling and Analysis of Hypersonic Structures Under Combined Loading," *52nd AIAA/ASME/ASCE/AHS/ASC Structures, Structural Dynamics and Materials Conference*, AIAA Paper 2011-1965, April 2011.

[39] DeCarlo, E. C., Mahadevan, S., and Smarslok, B. P., "Bayesian Calibration of Aerothermal Models for Hypersonic Air Vehicles," *54th AIAA/ASME/ASCE/AHS/ASC Structures, Structural Dynamics, and Materials Conference*, AIAA Paper 2013-1683, 2013, pp. 1–16.

[40] Smarslok, B. P., and Culler, A. J., "Error Quantification and Confidence Assessment of Aerothermal Model Predictions for Hypersonic Aircraft," *AIAA/ASME/ASCE/AHS/ASC Structures, Structural Dynamics and Materials Conference*, AIAA Paper 2012-1817, April 2012.

[41] Murphy, K. P., "Conjugate Bayesian Analysis of the Gaussian Distribution," Technical Rept., Univ. of British Columbia, Vancouver, BC, 2007, http://citeseerx.ist.psu.edu/viewdoc/summary?doi=10.1.1.126.4603.

R. Ghanem
Associate Editor